Bioactive Materials 43 (2025) 441–459

Contents lists available at ScienceDirect

Bioactive Materials

journal homepage: www.keaipublishing.com/en/journals/bioactive-materials

Injectable double-crosslinked bone cement with enhanced bone adhesion and improved osteoporotic pathophysiological microenvironment for osteoregeneration in osteoporosis

Lingfei Zhao [a,b], Chenyu Liu [a,b], Xing Chen [a,b], Zirui He [a,b], Shuiquan Zhang [a,b], Anan Zhang [a,b], Shuaimin Tang [a,b], Zihan Wu [d,**], Changsheng Liu [a,b,c,***], Yuan Yuan [a,b,c,*]

[a] Key Laboratory for Ultrafine Materials of Ministry of Education, and School of Materials Science and Engineering, East China University of Science and Technology, Shanghai, 200237, PR China
[b] Frontiers Science Center for Materiobiology and Dynamic Chemistry Engineering Research Center for Biomedical Materials of Ministry of Education East China University of Science and Technology, Shanghai, 200237, PR China
[c] Engineering Research Center for Biomedical Materials of Ministry of Education, East China University of Science and Technology, Shanghai, 200237, PR China
[d] Shanghai Rebone Biomaterials Co., Ltd, Shanghai, 201707, PR China

ARTICLE INFO

Keywords:
Injectable bone cement
Double crosslinked network
Bone adhesion
Bone homeostasis
Osteoclastogenesis
Osteoporotic bone regeneration

ABSTRACT

The osteoporotic bone defect caused by excessive activity of osteoclasts has posed a challenge for public healthcare. However, most existing bioinert bone cement fails to effectively regulate the pathological bone microenvironment and reconstruct bone homeostasis in the presence of osteoclast overactivity and osteoblast suppression. Herein, inspired by natural bone tissue, an in-situ modulation system for osteoporotic bone regeneration is developed by fabricating an injectable double-crosslinked PEGylated poly(glycerol sebacate) (PEGS)/calcium phosphate cement (CPC) loaded with sodium alendronate (ALN) (PEGS/CPC@ALN) adhesive bone cement. By incorporating ALN, the organic-inorganic interconnection within PEGS/CPC@ALN results in a 100 % increase in compression modulus and energy dissipation efficiency. Additionally, PEGS/CPC@ALN effectively adheres to the bone by bonding with amine and calcium ions present on the bone surface. Moreover, this in-situ regulation system comprehensively mitigates excessive bone resorption through the buffering effect of CPC to improve the acidic microenvironment of osteoporotic bone and the release of ALN to inhibit hyperactive osteoclasts, and facilitates stem cell proliferation and differentiation into osteoblasts through calcium ion release. Overall, the PEGS/CPC@ALN effectively regulates the pathological microenvironment of osteoporosis while promoting bone regeneration through synergistic effects of drugs and materials, thereby improving bone homeostasis and enabling minimally invasive treatment for osteoporotic defects.

1. Introduction

The prevalence of osteoporosis and bone-related diseases has been steadily increasing in recent years, particularly among females aged over 50 and males aged over 65 years [1]. Osteoporosis, which is mainly caused by the excessive differentiation of osteoclasts, significantly contributes to bone damage and consequently imposes a considerable social and economic burden on the patient [2–4]. Aging and estrogen deficiency lead to excessive accumulation of inflammatory mediators, such as interleukin-6 (IL-6) and tumor necrosis factor-α (TNF-α), within the microenvironment, triggering the hyperdifferentiation of osteoclasts [5,6]. This excessive activity of osteoclasts causes continuous degradation of the bone matrix via the secretion of abundant H^+ and cathepsin K (CTSK), further exacerbating the imbalance in receptor activator of

Peer review under responsibility of KeAi Communications Co., Ltd.
* Corresponding author. Key Laboratory for Ultrafine Materials of Ministry of Education, and School of Materials Science and Engineering, East China University of Science and Technology, Shanghai, 200237, PR China.
** Corresponding author.
*** Corresponding author. Key Laboratory for Ultrafine Materials of Ministry of Education, and School of Materials Science and Engineering, East China University of Science and Technology, Shanghai, 200237, PR China.
E-mail addresses: wuzihan@rebone.com (Z. Wu), liucs@ecust.edu.cn (C. Liu), yyuan@ecust.edu.cn (Y. Yuan).

https://doi.org/10.1016/j.bioactmat.2024.09.032
Received 22 May 2024; Received in revised form 22 September 2024; Accepted 23 September 2024

nuclear factor kappa-B ligand/osteoclastogenesis inhibitory factor (RANKL/OPG) expression and creating a vicious cycle of osteoclast differentiation under receptor activator of nuclear factor kappa-B (RANK) stimulation [7]. The dysregulation of bone homeostasis caused by hyperdifferentiated osteoclasts results in microstructural damage [8,9], increased bone fragility [10], and reduced bone strength in individuals with osteoporosis, significantly elevating their susceptibility to fragility fractures [11]. Meanwhile, deteriorating bone homeostasis not only enhances the adipogenic differentiation capacity of mesenchymal stem cells but also accelerates the breakdown metabolism of newly formed bone calluses, thereby hindering the generation of bone bridging at defective sites and significantly impairing bone regenerative capabilities [12]. Osteoporotic bone defects pose a significant threat to the skeletal health and life security of elderly patients, thereby presenting a critical challenge in the field of orthopedic surgery that cannot be disregarded [13]

Currently, the primary treatment modalities for osteoporotic bone defects include open surgery, long-term drug therapy, and minimally invasive treatment [14]. Open surgery poses challenges such as compromised internal fixation stability, increased susceptibility to secondary fractures, and increased disability and mortality rates [15]. Long-term drug therapy may induce adverse effects including atypical femoral fractures, renal impairment, and immune dysfunction [1]. Minimally invasive treatments have gained widespread adoption owing to their low invasiveness and ability to reduce patient discomfort. Injectable nanoparticles and bone cements are commonly utilized for treating osteoporotic bone defect in minimally invasive treatments [16–18]. The exceptional tissue penetration and expansive surface area of nanoparticles offer the potential for the precise modulation of microenvironments in osteoporotic bone defects [19]. However, their applications are limited by their low effective concentrations and inadequate targeting [20,21]. The low mechanical performance and carrier dependency nanoparticles also hinder the clinical applications of nanoparticles [22]. Although injectable bone cements offer advantages such as high operability, spontaneous in vivo conformation, and easy curability, existing bone cements such as poly(methyl methacrylate) (PMMA) cements and calcium phosphate cements (CPC) suffer from drawbacks such as inappropriate mechanical strength, inadequate tissue adhesion, low bioreactivity, and degradation rates mismatching bone regeneration rates, resulting in suboptimal bone repair outcomes [23–26]. Addressing prominent challenges associated with weak repair capability for osteoporotic bone defects and significant surgical trauma, the development of novel injectable bone cements has paramount importance for achieving the precise in situ modulation of osteoporotic bone regeneration, necessitating suitable mechanical strength, robust tissue adhesion, and high bioreactivity [27,28].

PEGylated poly(glycerol sebacate) (PEGS), a biodegradable polymer derived from poly(glycerol sebacate), exhibits excellent biocompatibility and viscoelastic properties similar to those of human tissue [29]. Its ease of modification allows its extensive use in tissue engineering, including applications such as bone tissue repair and regeneration [30–32]. Sodium alendronate (ALN), a third-generation bisphosphonate drug, is widely prescribed for treating clinical osteoporosis [33–35]. ALN can mitigate osteoclast activity, suppress bone resorption, indirectly stimulate osteoblasts, and increase bone mass [36,37]. Currently, ALN is primarily administered via oral and injectable methods; however, the systemic administration of ALN faces challenges such as suboptimal effective concentration and inadequate targeting, resulting in an increased incidence of drug side effects and diminished efficacy in bone repair [38–40].

This study presents a comprehensive approach to addressing osteoporotic bone defects by focusing on microenvironmental characteristics of the osteoporotic bone. The utilization of L-lysine diisocyanate (LDI) crosslinked PEGS, in combination with inorganic calcium phosphate cement (CPC) and alendronate (ALN), offers a biomimetic strategy that mimics natural bone components. The fabricated PEGS/CPC@ALN injectable bone cement contains an organic–inorganic interpenetrating network, where the combination of PEGS and LDI forms an organic network and CPC forms the inorganic mineralized network. Moreover, the amino groups of ALN react with the isocyanate groups in the organic network to form a polyurea structure, and the bisphosphonate group of ALN chelate with calcium ions in the inorganic CPC network, thereby connecting and reinforcing both networks to enhance the mechanical performance of bone cement. This bone cement with dual interconnected networks provides mechanical support at bone defect sites. Furthermore, the bisphosphonate group of ALN chelate with calcium ions on the bone, and the isocyanate groups of LDI react with amino groups of the bone to form a polyurea structure, achieving dual physical/chemical strong bonding at bone defect sites. Additionally, the PEGS/CPC@ALN bone cement can regulate acidic microenvironment by using its calcium phosphate and releasing ALN into osteoclasts to expedite their apoptosis. This dual action of the PEGS/CPC@ALN bone cement effectively inhibits excessive osteoclast activity, thereby precisely modulating the osteoporotic bone regeneration microenvironment. Tartrate-resistant acid phosphatase (TRAP) staining and pH-sensing chemical probes show that the PEGS/CPC@ALN cement creates an advantageous microenvironment for treating osteoporosis (Scheme 1). Osteoporotic bone defect repair experiments conducted on ovariectomized Sprague–Dawley (SD) rats indicate that the PEGS/CPC@ALN cement exhibits commendable reparative capabilities for osteoporotic femoral defects. In conclusion, the PEGS/CPC@ALN cement is a novel method for treating osteoporotic bone defects, in which all components demonstrate high suitability for clinical translation. Consequently, the PEGS/CPC@ALN cement has promising prospects in clinical applications.

2. Materials and methods

2.1. Materials

All chemical reagents were used as received without any further purification. Poly(ethylene glycol) diglycidyl ether (PEGDGE; average Mn: 500 Da) was purchased from Sigma-Aldrich (Merck). N, N-dimethylformamide (DMF) was purchased from Shanghai Titan Scientific Co., Ltd. Calcium phosphate cement powder (Rebone, China) was composed of equimolar tetracalcium phosphate (TTCP, $Ca_4(PO_4)_2O$) and dicalcium phosphate anhydrous (DCPA, $CaHPO_4$). Alendronate (ALN; 97 %) was obtained from Aladdin Chemical Testing Co.,Ltd. Porcine skin and porcine bone were purchased from a local market. L-Lysine Diisocyanate (LDI) and other chemical reagents were purchased from Shanghai Aladdin Biochemical Technology Co., Ltd.

2.2. Synthesis of catalyst bis(tetrabutylammonium) sebacate (TBAS)

TBAS was synthesized to catalyze the epoxide ring-opening reaction. TBAS was prepared as previously reported with some modifications. In brief, sebacic acid (1.95 g, 1 equiv.) and tetrabutylammonium hydroxide (TBAH; 20 g, 2 equiv., ≈25 wt% in H_2O) were mixed in 100 mL of 95 % ethanol and stirred for 30 min at 55 °C. Then, the ethanol of the mixture was removed by rotary evaporation, and the residual water was removed by lyophilization. The resultant TBAS was obtained as a white powder and stored in a desiccator for further use.

2.3. Synthesis of PEGS

PEGylated poly(glycerol sebacate) (PEGS) was synthesized based on a TBAS-induced epoxide ring-opening reaction. To prepare PEGS, sebacic acid (10.11 g, 1 equiv.), PEGDGE (25 g,1 equiv.), and the catalyst TBAS (0.21 g, 0.006 equiv.) were mixed and homogeneously dissolved in 100 mL of anhydrous DMF in a glovebox filled with high-purity nitrogen. Then the mixture was poured into a Schlenk flask, and the flask was transferred out of the glove box after sealing. The flask was

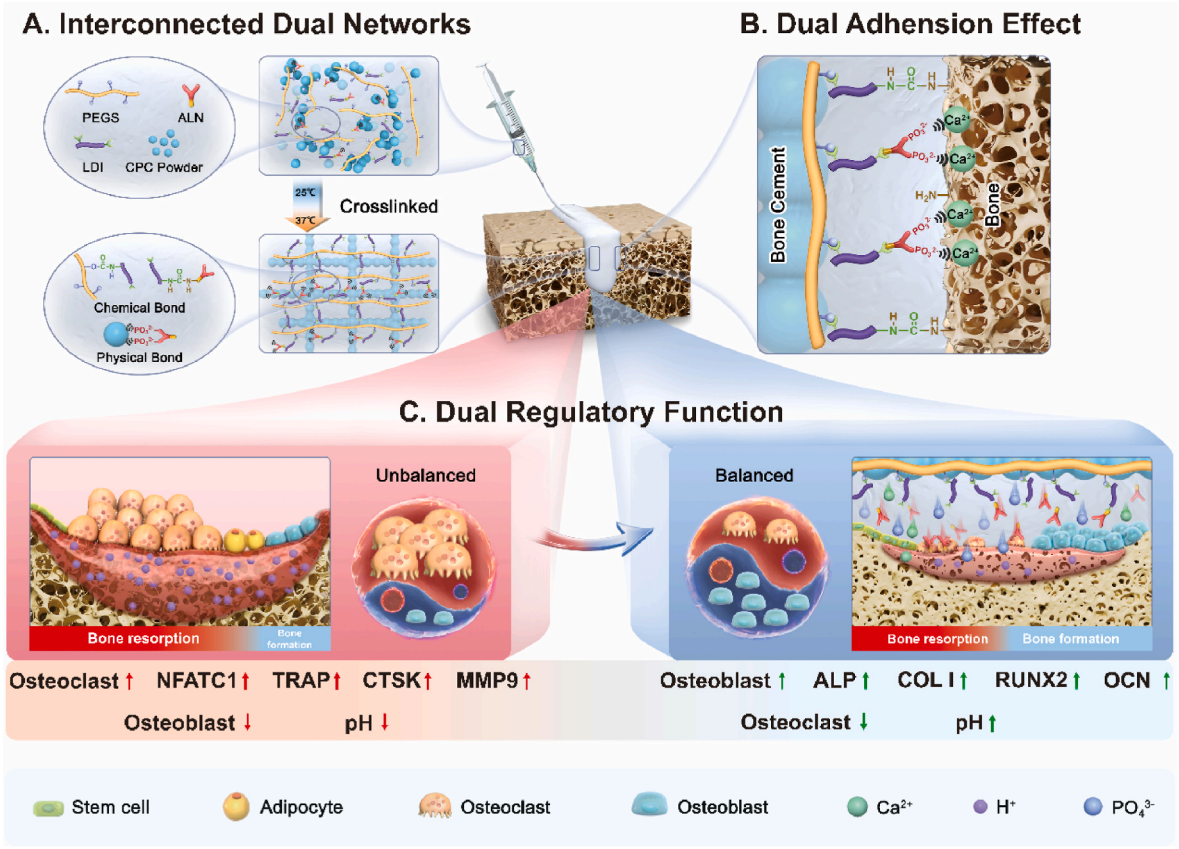

Scheme 1. Design of the antiosteoporotic bone cement for osteoporotic bone defect repair. A) The polymer network consists of PEGS crosslinked via LDI, while the inorganic network forms upon the hydration of CPC. Both networks are interlinked under the influence of ALN. B) Upon injection of the antiosteoporotic bone cement slurry into the site of osteoporotic bone defect, covalent bonds and electrostatic interactions are formed at the interface between the antiosteoporotic bone cement and bone. C) By modulating the bone microenvironment and inhibiting excessive differentiation of osteoclasts, the antiosteoporotic bone cement facilitates the regeneration of osteoporotic bone.

connected to a Schlenk line and heated to 100 °C in an oil bath. After 72 h of continuous stirring under a nitrogen atmosphere, the mixture was precipitated in pre-cooled ethyl ether and dried overnight at ambient temperature under vacuum to obtain crude PEGS. The crude PEGS was dialyzed (MWCO: 3500; Viskase, USA) against water for 24h and ethanol for 24h to remove residual small molecules. The resultant purified PEGS solution was dried under vacuum.

2.4. Molecular structural characterization

Molecular Structural Characterization: The chemical structures of the synthesized compounds were confirmed by using proton nuclear magnetic resonance (^{1}H NMR) spectroscopy (Bruker Ascend 600 MHz, Bruker Corporation, Switzerland) in dimethyl sulfoxide-d6 (DMSO-d6) for TBAS and PEGS. The resultant data were processed and analyzed with MestReNova software. Fourier transform infrared spectra (FTIR, Nicolet 5700, Thermo Scientific, USA) of all the synthesized compounds were recorded in the range of 500–4000 cm^{-1}. The molecular weight (M_n) and polydispersity index (PDI) of PEGS were evaluated by using gel permeation chromatography (GPC; Shimadzu Prominence HPLC instrument, Kyoto, Japan) with DMF as the eluent and polystyrene as the standard.

2.5. Rheological studies of the PEGS/CPC bone cement slurry

To evaluate the rheological properties of the bone cement slurries with different mass ratio of PEGS to CPC, a HAAKE MARS III rotational rheometer with a parallel plate (P20 TiLS, 20 mm in diameter) was used to measure the viscosity of the slurries. All tests were performed at 25 °C and the gap of the parallel plate was fixed at 1 mm. After 600 μL of homogeneous bone cement slurries were injected between the parallel plate, oscillatory time sweep tests were immediately performed to evaluate the viscosity of the bone cement slurries with 1 % constant strain and 10 Hz constant frequency. The viscosity–time curve was recorded. All the tests were repeated four times for each group.

2.6. Preparation and characterization of the antiosteoporotic bone cements

The antiosteoporotic bone cement is composed of PEGS, CPC, LDI, and ALN, prepared using a commonly employed clinical technique of uniform blending. Specifically, after preliminary screening, PEGS and CPC are weighed in a mass ratio of 2:8, followed by thorough mixing. Subsequently, LDI and ALN are added, with LDI comprising two components. CPC, PEGS, LDI and ALN were mixed and stirred in a small disk, meanwhile, the mixture was ultrasound for 5 min. The first component serves for cross-linking PEGS, with the quantity determined based on a ratio of the theoretical isocyanate groups on LDI to the hydroxyl groups on PEGS at 1.25:1. The second component is utilized for linking ALN, with the quantity determined based on a ratio of the theoretical isocyanate groups on LDI to the amino groups on ALN at 1:1.25. By varying the amounts of ALN and additional LDI, five main antiosteoporotic bone cements with different drug loading capacities were prepared, designated as A_0, A_1, A_2, A_3, and A_4, as detailed in Table S1 (Supporting Information). The functional groups and crystalline structures of the cement specimens were examined with using FT-IR spectra (Nicolet 5700, ThermoScientific) and X-ray diffraction (XRD, Rigaku D/Max2550, Cu Karadiation, Japan). The thermogravimetric analysis

(TGA) were obtained on a simultaneous thermal analysis (STA, STA449F5, Germany) under an N_2 atmosphere from room temperature up to 800 °C at a rate of 10 °C min^{-1}.

2.7. Rheological studies and the dynamic thermal behavior of the antiosteoporotic bone cements

To evaluate the rheological properties of the bone cements with different components, a HAAKE MARS III rotational rheometer with a parallel plate (P20 TiLS, 20 mm in diameter) was used to measure the curing kinetics of the bone cements. All tests were performed at 37 °C and the gap of the parallel plate was fixed at 1 mm. After 600 μL of homogeneous bone cement slurries were injected between the parallel plate, oscillatory time sweep tests were immediately performed to evaluate the curing kinetics of the bone cements with 1 % constant strain and 10 Hz constant frequency. The curing points were determined as the intersection points of the storage moduli (G′) and loss moduli (G″) curves. All the tests were repeated four times for each group. During injection and solidification, thermal photographs of the bone cements were taken by an IR thermal camera (FOTRIC 220S, China). The temperature evolutions at different time intervals were recorded and analyzed with Magnity Electronics tools systems.

2.8. Mechanical studies of the antiosteoporotic bone cements

To evaluate the mechanical properties of the bone cements with different components, an electronic mechanical testing machine (SANS CMT2503) equipped with a 5000 $_N$ load cell was used to measure the compressive properties and fatigue resistance of the completely cured bone cements. According to ISO 5833: 2002, the compression test and the fatigue resistance test were conducted at a constant displacement rate of 20 mm min^{-1}. Each sample (n = 4) was prepared by mixing vigorously the powders and curing fluids for 60 s until uniformity was achieved. Then these pastes were injected into molds. Cylindrical Teflon molds (Ø 6 × 12 mm) were selected for the compression experiment. After extrusion of the paste, all specimens were placed to cure at room temperature. After setting, each sample was de-molded and undesirable samples (presence of cracks and defects) were removed from the experiment. The ultimate compressive stress–strain tests were used to evaluate the compressive strength and strain at break. Cyclic loading–unloading compressive tests (10 cycles) at a compressive distance of 2 mm were used to evaluate the fatigue resistance. Cyclic loading–unloading tests were also used to assess the EDE (%) of the bone cement. The EDE was calculated according to the following equation:

$$\mathrm{EDE} = \frac{S_1}{S_1 + S_2} \times 100\% \quad (1)$$

where S_1 is the area of the hysteresis loop between the loading curves and unloading curves, and S_2 is the area under the unloading curves. All the tests were repeated four times for each group.

2.9. In vitro degradation of the antiosteoporotic bone cements

The antiosteoporotic bone cement of all groups (n = 3) were soaked a Tris–HCl (pH = 7.4) buffer solution with the addition of esterase at the concentration of 0.625 unit/mg PGS and PEGS at 37 °C. The solution was refreshed every 3 days. At various time points, the cements were removed from the solution, washed with deionized water and dried in a blast dryer at 70 °C for 4 h. The weight loss was calculated as the following equation:

$$\text{Weight loss ratio} = \frac{w_0 - w_t}{w_0} \times 100\% \quad (1)$$

where w_0 indicates mass of undegraded sample, w_t indicates mass of the sample for the corresponding time of degradation.

2.10. Adhesive properties of the antiosteoporotic bone cements

Initially, we conducted fracture bonding experiments to assess the anti-washout properties of the antiosteoporotic bone cements. The bonded bone tissues were weighed, with the initial mass recorded as w0. Subsequently, continuous water flow impact was applied, halted at predetermined intervals, followed by drying and mass measurement recorded as wt. The residual mass calculation rate is defined as:

$$\text{Residual mass ratio} = \frac{w_0 - w_t}{w_0} \times 100\% \quad (1)$$

To evaluate the adhesive properties of the antiosteoporotic bone cements in bone tissue and soft tissue, an electronic mechanical testing machine (SANS CMT2503) equipped with a 5000 N load cell was used to measure the lap-shear strength and interfacial toughness. All tests were conducted at a constant displacement rate of 50 mm min^{-1}. Lap-shear tests were used to evaluate the lap-shear strength according to ASTM F2255 with some modifications. For the lap-shear tests, 500 μL of samples were injected into the adhesion region of the bone tissue, and the adhesion area was fixed to 30 mm width × 15 mm length. The lap-shear strength was calculated according to the following equation:

$$\text{Lap} - \text{shear strength} = \frac{F_L}{w_1 \times l_1} \quad (2)$$

Where F_L is the maximum force during shearing, and w_1 and l_1 are the width and length of the adhesion area respectively.

The adhesive performance of the antiosteoporotic bone cements can be influenced by both the moist bone tissue environment and the release of ALN during in vivo application. To further investigate this, the bone adhesive strength of the antiosteoporotic bone cements under conditions that simulate the complex in vivo environment was tested. Specifically, bone tissue samples were immersed in PBS solution (pH = 7.4) to ensure moisture saturation, then immediately adhered with the antiosteoporotic bone cements. After the cements cured, the adhesion area (30 mm width × 15 mm length) was kept moist condition by using PBS, and tensile tests were conducted at specific time points to measure the lap-shear strength.

Next, 180° peeling tests were used to evaluate the interfacial toughness according to ASTM F2256 with some modifications. For the 180° peeling tests, 1 mL of samples were injected into the adhesion region of the soft tissue, and the adhesion area was fixed to 20 mm width × 40 mm length. The interfacial toughness was calculated according to the following equation:

$$\text{Interfacial toughness} = \frac{2 \times F_{plateau}}{w_2} \quad (3)$$

where $F_{plateau}$ is the plateau force during peeling, and w_2 is the width of the adhesion area. All the tests were repeated four times for each group.

2.11. Cytocompatibility evaluation of the antiosteoporotic bone cements

To evaluate the cytocompatibility of the antiosteoporotic bone cements, co-culture experiments were conducted between bone cement leachate and L929 cells following ISO 10993–5:2009 guidelines. Prior to testing, the cured bone cement was sterilized by UV irradiation for 24 h. Meanwhile, complete growth medium was prepared by supplementing Dulbecco's Modified Eagle Medium (DMEM; Gibco) with 10 % fetal bovine serum (Gibco), 1.0 × 10^5 U L^{-1} penicillin (HyClone), and 100 mg L^{-1} streptomycin (HyClone). The bone cement was immersed in the complete growth medium at a concentration of 200 mg mL^{-1} to ensure full immersion and incubated for 24 h at 37 °C in a 5 % CO_2 incubator. After 24 h, the leachate was obtained. L929 cells were seeded in a 96-well plate at a density of 10,000 cells/well, with empty wells serving as blank. The cells were cultured in complete growth medium at 37 °C in a 5 % CO_2 environment for 24 h before being exposed to the leachate for

another 24 h. Following exposure, the culture medium was removed, and 50 μL of MTT solution (1 mg mL^{-1}) was added to each well. The plate was then incubated at 37 °C in a 5 % CO_2 environment for 2 h, followed by dissolution of the formed formazan crystals using isopropanol. Absorbance was measured at 570 nm using a microplate reader (Spectra Max $M2^e$, Molecular Devices, USA). Cell viability was calculated and obtained based on previous studies [41]. For live/dead staining assay, bone marrow-derived macrophages were co-cultured with the antiosteoporotic bone cements for 7 days, and then replaced with the calcein-AM/PI double stain kit (Beyotime, China) for 30 min. The samples were observed and imaged by using an inverted ffuorescence microscope (Olympus, IX71, Japan). To assess the short-term biocompatibility, the antiosteoporotic bone cements were implanted into femoral defects of Sprague-Dawley (SD) rats. The femurs and major organs were extracted on days 1, 2, 3, 4, and 5, and subsequently processed and stained with hematoxylin and eosin (HE) to evaluate the biocompatibility of the antiosteoporotic bone cements. All procedures followed the National Institute of Health Guide for the Care and Use of Laboratory Animals and were approved by the Shanghai Rat & Mouse Biotech., LTD (approved number: 20240630(09)).

2.12. In vitro ALN release

Since the ALN is not UV active, the concentration of ALN was derivatized with FMOC to form a UV-active component using a modified method reported by Van Houdt et al. [42]. Briefly, the ALN release experiments in vitro were conducted by soaking the antiosteoporotic bone cements in PBS (5 mL, pH = 7.4) and incubating them in a shaker at 37 °C. At the predetermined time points, the resulting solution (1 mL) was collected for detection and an equal amount of fresh PBS was added to the release medium. 100 μL of resulting solution was pipetted in a 96-well plate, after which 75 μL of ninhydrin color reagent (Sigma-Aldrich, St. Louis, USA) was added for incubation at 80 °C for 30 min Subsequently, the well plate was cooled and 100 μL of stabilizing solvent (50 % ethanol) was added into each well. The absorbance of each well was measured on a microplate spectrophotometer at 570 nm (Bio-Tech Instruments, Winooski, VT, USA).

2.13. In vitro buffering effect

The A_1 to A_3 bone cements were formed into cylindrical shapes (Ø 6 × 12 mm), placed into PBS buffer (pH = 4), and uniformly stirred using a magnetic stirrer (Cimarec, Thermo Scientific, USA) at 37 °C. At various time points, 2 mL of reaction solution was extracted and immediately replenished with an equal volume of PBS buffer at the same pH. Subsequently, the pH of the reaction solution was measured using a pH meter and recorded.

2.14. Osteoclastic-inhibition effects of the antiosteoporotic bone cements

For osteoclast formation, the bone cements were immersed in ***α***-MEM medium, followed by the addition of fetal bovine serum (FBS, 10 %), streptomycin (100 mg mL^{-1}), and penicillin (100 U mL^{-1}) to prepare the complete medium. Bone marrow-derived macrophages were obtained from 6-week-old Sprague Dawley (SD) rat and seeded into 24-well plates at a density of 1×10^5 cells/well. They were then cultured for osteoclast differentiation in the presence of RANKL (75 ng mL^{-1}) and M-CSF (30 ng mL^{-1}). During the co-cultivation of the bone cements and osteoclasts, the collected culture medium from media changes was gathered, and its pH value was measured. After 5 days of culture, the cells were fixed with 4 % paraformaldehyde and stained. For TRAP staining, using the TRAP staining kit (Sigma-Aldrich, USA). TRAP-positive multinucleated cells (nuclei ≥3) were identified as osteoclasts and counted. For F-actin ring fluorescence staining, cells were stained with FITC-phalloidin for F-actin and 4′,6-diamidino-2-phenylindole (DAPI) for nuclei. Then three patterns of podosome, including podosome clusters, actin rings, and podosome belts, were counted. For pH detection, cells were stained with pH probe (AIE, China).

2.15. Ca^{2+} release of the antiosteoporotic bone cements

The dynamic release of Ca^{2+} from the bone cements was investigated. Briefly, samples from all groups were immersed in 5 mL PBS solution (pH = 7.4). The soaking solution was collected at regular intervals. The concentration of Ca^{2+} in the immersion solution was measured using an inductively coupled plasma atomic emission spectrometer (ICP-AES, PerkinElmer Optima 2000, USA).

2.16. Osteogenic differentiation effects of the antiosteoporotic bone cements

The Cell Counting Kit-8 (CCK-8, Beyotime, China) assay was also employed to assess cell growth. BMSCs were seeded onto samples of each bone cement group in a 24-well culture plate at a density of 4×10^4 cells/well in α-MEM medium. After culturing for 4 and 7 days, the medium was replaced with α-MEM medium containing 10 % CCK-8. Subsequently, the cells were incubated at 37 °C in 5 % CO_2 for analysis, and absorbance at 450 nm was measured using a microplate reader (Epoch, BioTek Instruments, Inc.).

For ALP and ARS staining, BMSCs were seeded at a density of 1×10^5 cells/well onto the surface of bone cement in 24-well plates and cultured with osteogenesis differentiation medium (***α***MEM medium supplemented with 10 % FBS, 10 nm vitamin D, 10 mm ***β***-glycerolphosphate, 10 nm dexamethasone, 100 mg mL^{-1} streptomycin, and 100 U mL^{-1} penicillin). Following culture for 14 and 21 days, ALP staining and ARS staining were conducted using a BCIP/NBT ALP Color Development Kit (Beyotime Biotechnology, China) and an ARS solution (Cyagen Bioscience, China), respectively. Visualization was performed using a stereo microscope (Leica, Germany). Additionally, ALP activity was assessed using an ALP activity assay kit (Beyotime Institute of Biotechnology, China).

2.17. RNA analysis using qRT-PCR

Total RNA extracts were obtained through the lysis of osteoclasts and BMSCs with Trizol (TAKARA, Japan) after three days of treatment following the manufacturer's instructions. The purity and concentration were quantified using NanoDrop 2000 (Invitrogen, USA). Reverse transcription was performed using PrimeScript RT reagent kit (TAKARA, RR037A) following the manufacturer's instructions. PCRs were performed using TB Green Premix Ex Taq kit (TAKARA, RR420A), following the manufacturer's instructions. The primer sequences used are listed in Table S2 (Supporting Information).

2.18. Osteoporotic bone defect repair

Osteoporosis is a typical age-related disease, and selecting 12-month-old SD rats allows for a better mimicry of the complex bone microenvironment associated with aging and estrogen deficiency. The bone defect model provides a more accurate simulation of the clinical application of bone cement. In contrast to the fracture model, which involves a more complex bone microenvironment, the bone defect model offers a clearer assessment of the therapeutic efficacy of the antiosteoporotic bone cements. All procedures followed the National Institute of Health Guide for the Care and Use of Laboratory Animals and were approved by the Shanghai Rat & Mouse Biotech., LTD (approved number: 20230301 (7)). To induce osteoporosis in female SD rats, ovariectomy surgery was performed on 12-month-old rats, followed by a 12-week period of rearing to establish the osteoporotic SD rat model [43]. To assess the osteogenic efficacy of the antiosteoporotic bone cements, a rat distal femoral defect model was employed. Twenty-five rats weighing between 300 and 350 g were randomly divided into 5 groups as follows: 1) Blank

(n = 5), 2) CPC (n = 5, injected with CPC bone cement), 3) A_0 (n = 5, injected with A_0 bone cement), 4) A_3 (n = 5, injected with A_3 bone cement), and 5) PMMA (n = 5, injected with PMMA bone cement). All female rats were anesthetized via intraperitoneal injection of pentobarbital (35 mg kg^{-1}). Subsequently, a defect with a diameter of 2 mm was created using an electric drill, and different bone cements were injected into the defects. Finally, the incisions were closed layer by layer. Rat femurs were collected at 6 and 12 weeks after surgery. Each femur sample was harvested and fixed in 4 % paraformaldehyde. To determine new bone formation, samples were scanned using a micro-CT system, and 3D images were reconstructed. For histological analysis, the femur samples were sequentially fixed with 4 % neutral paraformaldehyde, decalcified using ethylenediaminetetraacetic acid (0.5M), dehydrated in ethanol, and embedded in paraffin or PMMA. Subsequently, the femur samples were cut into 4.5 μm thin sections for H&E staining, Masson's staining, COL I staining, TRAP staining and immunohistochemistry (IHC) staining, and bone repair at the bone defect site was observed. Homologous, the main organs were also embedded in paraffin, sliced and stained by hematoxylin and eosin staining.

2.19. Statistical analysis

Statistical analysis in this study was performed using embedded algorithms in the commercial software GraphPad Prism 8. All results are represented as mean ± standard deviation. All analyses were conducted using one- or two-way analysis of variance (ANOVA) with post hoc analysis. A value of $p < 0.05$ was considered statistically significant and ns represents no significance (*$p < 0.05$, **$p < 0.01$, ***$p < 0.001$, and ****$p < 0.0001$).

3. Results and discussions

3.1. Fabrication and characterization of the antiosteoporotic bone cements

To fabricate the antiosteoporotic bone cement with dual interconnected networks and clinically relevant bone adhesion properties, firstly, a catalyst bis(tetrabutylammonium) sebacate (TBAS) was synthesized according to a previously reported method (Fig. S1A, Supporting Information) [41]. Subsequently, using TBAS as a catalyst, epoxy ring-opening polymerization was performed under acidic conditions to synthesize PEGS (Fig. S1B, Supporting Information). The structural characterization of TBAS and PEGS were performed via proton nuclear magnetic resonance (^{1}H NMR) spectroscopy (Figs. S2A and S2B, Supporting Information). The ^{1}H NMR spectrum of PEGS shows distinct peaks corresponding to decanedioic acid, glyceric acid, and PEG. Notably, the absence of epoxy proton signals (δ ≈ 3.00 ppm) from the ^{1}H NMR spectrum of PEGS indicates the complete participation of epoxy functional groups in the reaction. Further structural characterization of PEGS was performed via Fourier transform infrared (FTIR) spectroscopy (Fig. S3, Supporting Information). The FTIR spectrum of PEGS shows characteristic stretching vibration peaks at 2950 cm^{-1}, 1750 cm^{-1}, and 1200 cm^{-1}, corresponding to methylene groups (–CH_2–), carbonyl groups (–C=O), and ether groups (–C–O–C–), respectively, thereby confirming the presence of decanedioic acid, polyester, and PEG in PEGS [44]. Additionally, a broad and intense hydroxyl (–OH) stretching vibration peak is observed at 3500 cm^{-1} in the FTIR spectrum of PEGS, which robustly supports the presence of hydroxyl groups. Gel permeation chromatography (GPC) was performed to assess the molecular weight distribution of PEGS, which revealed a relatively narrow molecular weight distribution (Fig. S4, Supporting Information). In summary, ^{1}H NMR, FTIR, and GPC analyses collectively confirm the successful synthesis of PEGS with a narrow molecular weight distribution.

After the successful synthesis of PEGS, the antiosteoporotic bone cements were prepared using a method similar to the clinical bone cement formulation: thorough mixing. To ensure the injectability of the bone cements, the composite ratio of PEGS (liquid phase) and CPC (solid phase) was meticulously optimized. Fig. S5A (Supporting Information) shows that when the liquid phase content is higher than the solid phase content, the paste has low viscosity and good flowability, similar to pure PEGS. Conversely, as the solid phase content increases, the paste transitions toward a cement-like state with diminished flowability. Among the investigated cements with different PEGS/CPC ratios, the P2C8 bone cement (PEGS:CPC mass ratio = 2:8) exhibits optimal injectability without excessive fluidity, showing a toothpaste-like consistency after homogenization. Conversely, when the mass ratio of CPC in the bone cement reaches 90 %, PEGS fails to fully encapsulate the CPC powder, resulting in a composite entirely composed of a solid powder with no injectability, which is unsuitable for subsequent experimentation. Viscosity is a critical property of bone cement slurry, directly related to its injectability and subsequent stability. We used rheological analysis with an oscillatory time sweep method to test the viscosity of the aforementioned slurries. As Fig. S5B (Supporting Information) shows, it is evident that the viscosities of the P1C9, P4C6, P5C5, and P6C4 slurries are too low to stabilize and solidify at defect sites. The uncontrolled flow of bone cement poses significant health risks to patients. Compared to the P3C7 slurry, the P2C8 slurry exhibits higher viscosity, which, while maintaining injectability, reduces the likelihood of leakage from the injection site and presents a lower safety risk. These findings are consistent with the results shown in Fig. S5A (Supporting Information). Consequently, P2C8 was deemed as the optimal bone cement for further investigations.

After determining the ideal PEGS/CPC ratio, LDI and ALN were uniformly incorporated into the bone cement. In the presence of LDI, the internal polymer network of the bone cement undergoes crosslinking through the formation of covalent polyurethane bonds. Subsequently, upon binding with ALN, the internal polymer network of the bone cement integrates with the inorganic network of CPC via electrostatic interactions between phosphonate groups and calcium ions, thus achieving enhanced network connectivity. By varying the amounts of ALN and LDI, a series of antiosteoporotic bone cements with different drug contents were prepared. The mass fraction of LDI used for crosslinking PEGS in each group of the bone cement was 7.3 %, ensuring sufficient isocyanate groups to crosslink PEGS. Additionally, the mass ratio of ALN to excess LDI remains constant (ALN:excess LDI mass ratio = 1.198:1). After thorough mixing, the mixtures were cured in an oven at 37 °C. Based on the varying masses of added ALN, the prepared bone cements were named A_0, A_1, A_2, A_3, and A_4 (Table S1, Supporting Information).

Fig. 1A compares the FTIR spectrum of CPC with A_0, A_1, A_2, A_3, and A_4. In addition to the characteristic peaks of methylene, carbonyl, and ether bonds, the FTIR spectrum of PEGS also shows peaks at 3440 cm^{-1} and 1550 cm^{-1}, indicative of amide bonds (–NHCO–) in polyurethane structures. The presence of these peaks suggests the isocyanate groups of LDI can react with both the hydroxyl groups on PEGS and the amino groups on ALN. Furthermore, the absorption peak at 3480 cm^{-1} of N–H stretching vibrations in the FTIR spectra of A_1, A_2, A_3, and A_4 further corroborate the presence of ALN in these cements. The phase compositions of cured bone cements are shown in Fig. 1B. The addition of PEGS, ALN, and LDI does not significantly impact the inorganic components and crystalline structure of the bone cements. The X-ray diffraction (XRD) patterns of A_0, A_1, A_2, A_3, and A_4 exhibit the typical peaks of unhydrated tetracalcium phosphate (TTCP), similar to the XRD pattern of CPC, confirming the minimal influence of PEGS, LDI, and ALN on the cured product and crystal structure of the bone cements. Thermogravimetric analysis was performed to determine the ratio of organic and inorganic materials in the antiosteoporotic bone cements based on the significant difference in their thermal decomposition temperatures. As shown in Fig. 1C, the organic phase, comprising PEGS and LDI, initiates thermal degradation at 250 °C whereas the inorganic phase, comprising CPC and ALN, remains stable up to 800 °C. The mass loss rates remain

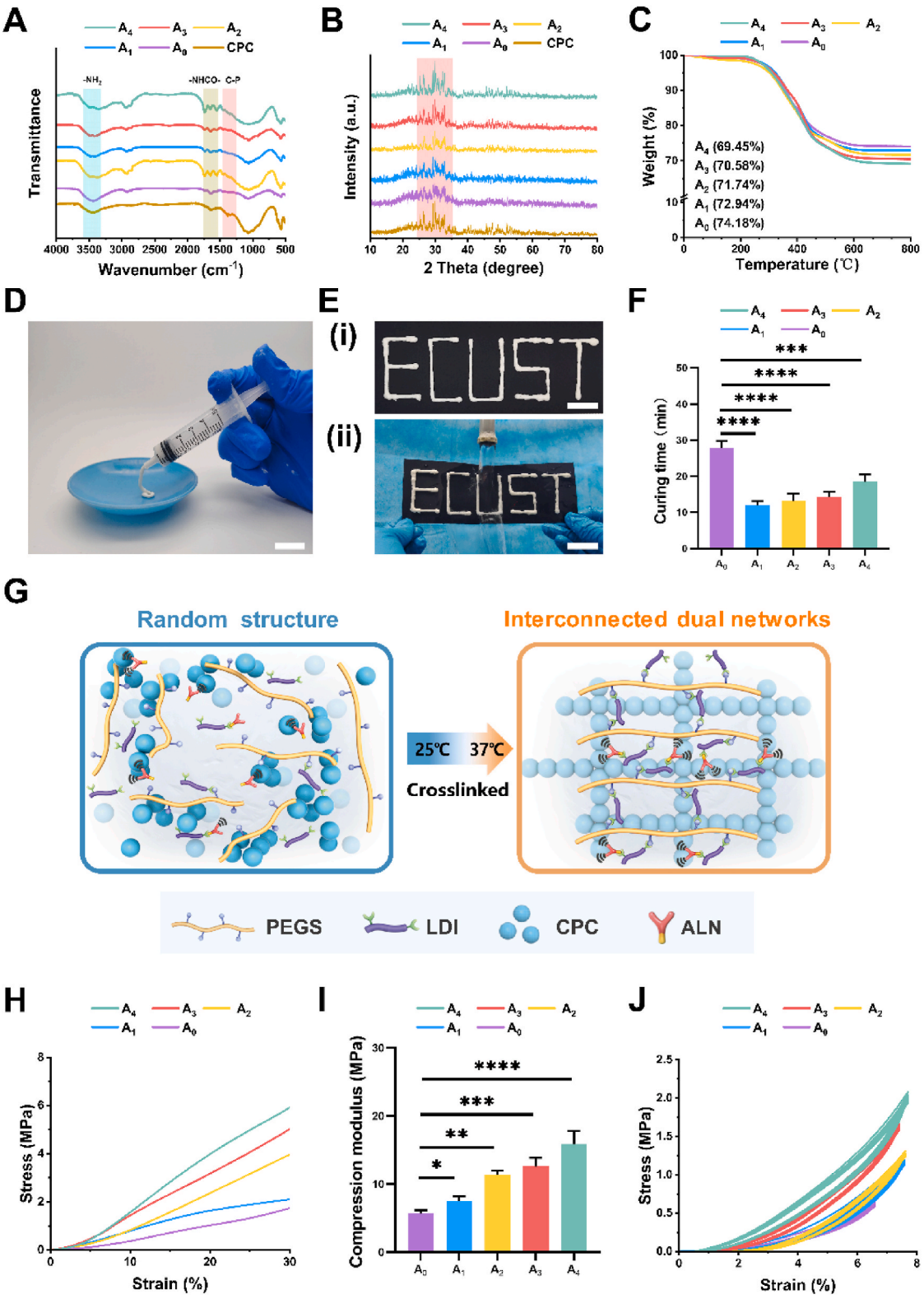

Fig. 1. Fabrication and characterization of the antiosteoporotic bone cements. A) FTIR spectra of CPC and the antiosteoporotic bone cements in the range of 500-4000 cm^{-1}. B) XRD patterns of the antiosteoporotic bone cements. C) TGA diagrams of the antiosteoporotic bone cements. D) Digital pictures of the injectability of the antiosteoporotic bone cements. Scale bar: 1 cm E) The plasticity (i, Scale bar: 1.5 cm) and resistance to washout properties (ii, Scale bar: 2 cm) of the antiosteoporotic bone cements. F) Curing time of the antiosteoporotic bone cements under 37 °C. G) Schematic representation of the design strategy for anti-osteoporotic bone cements with interconnected networks of polymer and inorganic materials. PEGS crosslinked via LDI constitutes the polymer network, while the inorganic network forms upon the hydration of CPC. Both networks are interconnected under the influence of ALN. H) Compressive stress–strain curves and I) modulus of the antiosteoporotic bone cements. J) Cyclic loading–unloading compressive curves of the antiosteoporotic bone cements at a compressive distance of 2 mm (10 cycles). (mean ± SD; n = 4; *$p < 0.05$; **$p < 0.01$; ***$p < 0.001$; ****$p < 0.0001$).

consistent with the organic phase feed ratio.

3.2. Injectability and mechanical properties of the antiosteoporotic bone cements

Clinical bone defects caused by osteoporosis have irregular shapes [44]. The injectability of the antiosteoporotic bone cements is a crucial property affecting its biomedical applications in bone repair, especially for irregular and complex bone defects [45]. As shown in Fig. 1D, the antiosteoporotic bone cements can be extruded using a syringe, demonstrating its excellent injectability. Fig. 1E(i) shows that the bone cement can be injected to form irregular and complex shapes, as required. Furthermore, the resistance of the bone cements to washout was examined via water jet tests (water pressure = 150–200 kPa), which reveals that the injected bone cement retains its shape under a water flow, indicating its good resistance to washout (Fig. 1E(ii) and Supplemental video 1). Additionally, we performed continuous washing experiments and dried the remaining bone cements at predetermined time points to weigh and calculate the residual mass proportion. As shown in Fig. S6 (Supporting Information), the antiosteoporotic bone cements demonstrated good anti-washout properties within 24 h. To evaluate the curing behavior of the antiosteoporotic bone cements, oscillatory time sweep tests were performed at the physiological temperature (37 °C). As shown in Fig. S7 (Supporting Information), the storage moduli (G′) of all antiosteoporotic bone cements increase with time, eventually surpassing the loss moduli (G″). The storage modulus of A_0 becomes constant after 40 min, and the storage moduli of A_1–A_4 become constant after 20 min. This indicates that the bone cement cures stably due to the action of the crosslinking agent LDI and ALN. Fig. 1F shows the curing time of the antiosteoporotic bone cements. A_0 has a curing time of up to 27 min, and A_1–A_4 have curing times of less than 20 min, with the shortest curing time of 12 min exhibited by A_1. These results indicate that ALN and LDI significantly shorten the curing time of the bone cements, implying that their introduction accelerates the curing of the bone cements, allowing more precise matching of the curing time with the clinical injection window. Notably, as the mass ratio of ALN and LDI increases, the curing time of the bone cement increases. This is because with an increase in the mass ratio of ALN, more amino groups compete with the hydroxyl groups of PEGS to react competitively with the isocyanate groups of LDI, reducing the amount of LDI available for forming polymer crosslinking networks and increasing the amount of LDI involved in linking with ALN, thus which increases the curing time of the bone cement from 12 min to 18 min. Adequate operational windows should be reserved for the clinical use of the bone cement to facilitate medical personnel operations while avoiding excessively slow curing time that may lead to uncured bone cement leakage in patients, potentially causing life-threatening thrombosis [46]. Temperature fluctuations during the solidification process of the bone cement serve as an indicator of its biocompatibility and gentleness towards biological tissues. Figs. S8A and S8B (Supporting Information) visually encapsulates the dynamic thermal behavior exhibited by bone cement during injection and curing process. As displayed in Supplemental video 2, initially, a modest elevation in temperature induced by shear force occurs, which remains well within the biologically tolerable range, thus safeguarding surrounding tissues from thermal damage. Subsequently, as the injection concludes, a gradual decline in temperature ensues, facilitating the stabilization of the cement matrix. The temperature profile reflects the biological solidification process of the bone cements, ensuring optimal compatibility with the physiological environment.

Supplementary data related to this article can be found online at https://doi.org/10.1016/j.bioactmat.2024.09.032

Once injected into the bone defect site and stably cured, the bone cement needs to withstand radial pressures [47]. Bone cement with certain mechanical strength and cohesion can provide long-term support at the bone defect site [48,49]. The formation of an inorganic network in CPC involves precursor hydration and dissolution, HA supersaturation and nucleation, followed by crystal growth and maturation. These processes collectively facilitate the formation of an inorganic network in CPC [50–53]. In the antiosteoporosis bone cements, the polymer network chemically crosslinked using partially introduced LDI exhibits elastic behavior with reversible deformation capability, and the inorganic network demonstrates high rigidity. ALN can not only form polyurea with LDI via its inherent amino groups to connect with the PEGS polymer network but also undergo electrostatic adsorption with the abundant Ca^{2+} in CPC through its inherent bisphosphonate groups to connect with the inorganic network. As shown in Fig. 1G, upon temperature elevation, dual interconnected networks can form within the bone cement. In particular, according to the requirements of ISO 5833:2002, compressive stress–strain tests were conducted to evaluate the compressive performance of the antiosteoporotic bone cements (Fig. 1H and Fig. S9 (Supporting Information)). Quantitative analysis reveals that with an increase in ALN and LDI contents in the bone cement, the compressive modulus of the bone cement increases, indicating that the addition of ALN and extra LDI not only interconnects the independent organic polymer network and inorganic calcium phosphate network but also makes the chemical crosslinking network denser. Under the joint action of these two mechanical reinforcement behaviors, the strength of the bone cement increases by 200 % (Fig. 1I). Furthermore, we investigated the mechanical performance of the antiosteoporotic bone cements within the pathological environment of osteoporosis. To simulate the pathophysiological environment, antiosteoporotic bone cements samples were immersed in PBS (pH = 5.5–6.0) for predetermined time intervals, after which their mechanical strength was assessed. As shown in Supporting Fig. S10 (Supporting Information), the mechanical properties of the antiosteoporotic bone cements did not exhibit a significant decline. At present, commonly used bone cements in clinical practice are PMMA and CPC. The compressive modulus of PMMA can generally reach 1.6 Gpa [54]. The high mechanical strength of PMMA does not match the surrounding bone tissue, which increases the risk of secondary fractures [55]. CPC has low compression modulus and brittleness [56]. This antiosteoporotic bone cements improves the toughness of CPC by adding PEGS organic network. Meanwhile, by connecting organic and inorganic networks together through ALN, the overall mechanical properties have been improved. Although the compressive performance of the bone cements was tested via stress–strain experiments, the bone cement implanted at the bone defect site would be subject to long-term dynamic pressures, increasing the demands for fatigue resistance. To evaluate the fatigue resistance of the antiosteoporotic bone cements, 10 cyclic loading–unloading compression tests were conducted, as shown in Fig. 1J. All bone cements could withstand ~7 % compression strain with a recovery rate of 100 %. The stress–strain curves of the cyclic loading–unloading tests almost completely overlap, indicating that all bone cements can maintain mechanical integrity under 7 % compression strain without disintegration. Furthermore, the 100-cycle compression test yielded similar conclusions. As shown in Fig. S11 (Supporting Information), the maximum point of each cycle was almost completely maintained at the same level, indicating that the antiosteoporotic bone cements exhibited an outstanding fatigue-resistant ability under a dynamic environment. Although the antiosteoporotic bone cements exhibits mechanical elasticity, significant differences are observed in their hysteresis loops. Quantitative analysis of their hysteresis loops (Figs. S12A and S12B, Supporting Information) shows that the energy dissipation efficiency (EDE) of A_1 is significantly higher than that of A_0, indicating that the introduction of ALN and excess LDI increases the EDE of the bone cement. This can be attributed to the introduction of ALN, which physically crosslinks the independent polymer and inorganic networks in the bone cement system. This dynamic and reversible electrostatic complexation undergoes fracture and recombination during loading and unloading to dissipate the force acting on the bone cement. With an increase in ALN and LDI contents, the degrees of electrostatic complexation and crosslinking gradually increase.

Therefore, reversible fracture and recombination of electrostatic complexes and free movement of segments are mechanically restricted within the bone cement with high chemical crosslinking, allowing the bone cement to maintain its mechanical integrity in complex mechanical environments, which is a disadvantage of rigid PMMA and brittle CPC bone cements.

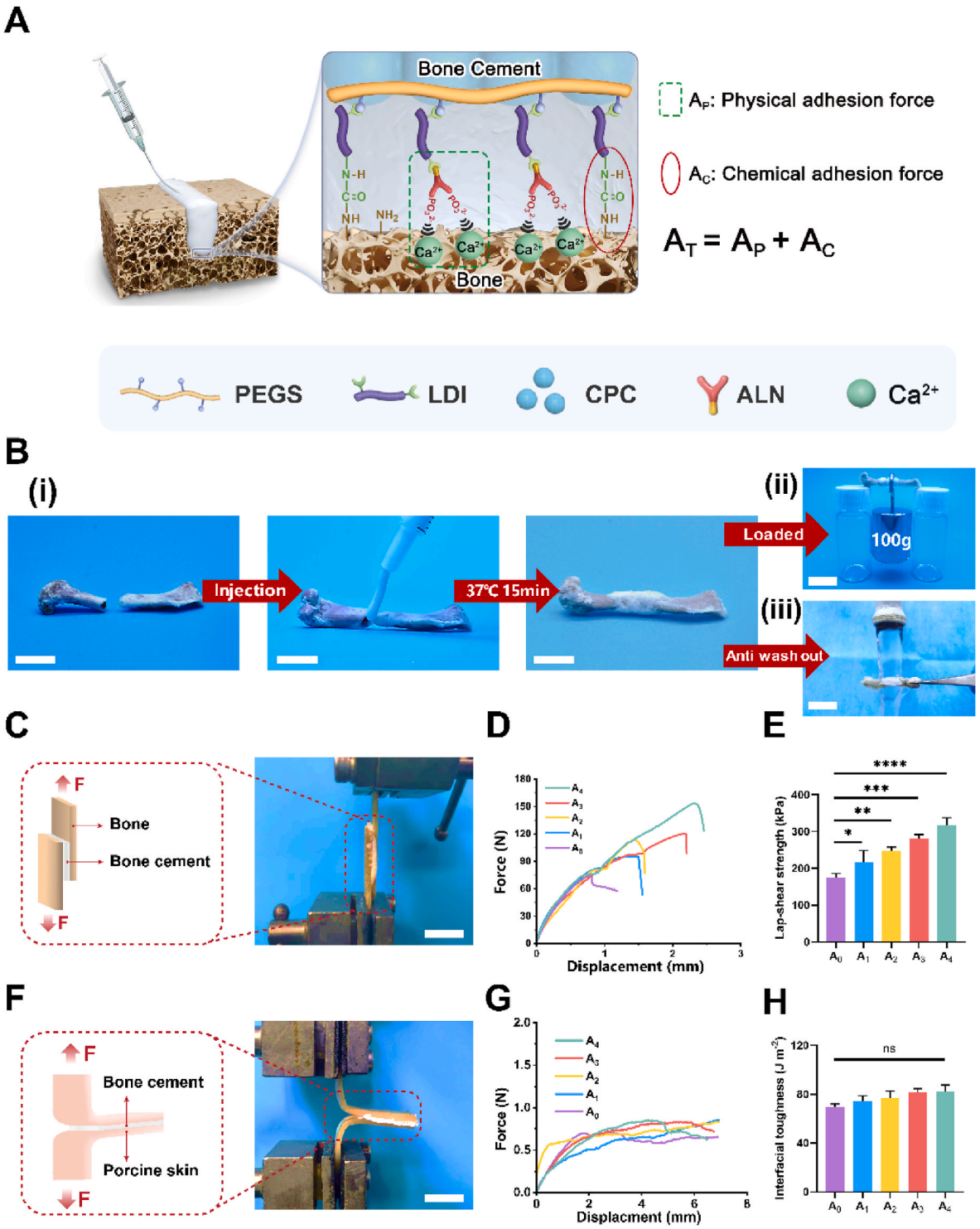

Fig. 2. Bone adhesion performance of the antiosteoporotic bone cements. A) Schematic representation of the dual adhesion mechanism of the antiosteoporotic bone cement to bone tissue. The total adhesion strength (A_T) is contributed by the chemical adhesion force (A_C) between LDI and amino groups on the bone tissue forming polyurea, and the physical adhesion force (A_P) between phosphonic groups and calcium ions on the bone tissue. B) Digital pictures of well-bonded bone tissue (i, Scale bar: 1 cm) and the stability of fully bonded bone tissue under the influence of 100g load (ii, Scale bar: 2 cm) and water flow (iii, Scale bar: 2 cm). C) Schematic representation and digital pictures of the lap-shear tests to bone. Scale bar: 2 cm. D) Typical force–displacement curves and E) lap-shear strength of the antiosteoporotic bone cements to bone. F) Schematic representation and digital pictures of the 180° peeling tests. Scale bar: 3 cm. G) Typical force–displacement curves and H) interfacial toughness of the antiosteoporotic bone cements to porcine skin. (mean ± SD; n = 4; *$p < 0.05$; **$p < 0.01$, ***$p < 0.001$; ****$p < 0.0001$).

3.3. Bone adhesion performance of the antiosteoporotic bone cements

In clinical scenarios, bone cements used for implantation often prioritize mechanical performance but overlook bone adhesion, a crucial aspect. The clinical use of the PMMA bone cement is frequently associated with excessive mechanical strength and poor bone tissue integration, leading to bone wear and secondary damage to patients [57,58]. Herein, this issue is addressed by using the amino groups on the collagen surface of the bone tissue and the abundant calcium ions on the hydroxyapatite surface as adhesive points. By leveraging the structural characteristics of LDI and ALN in the antiosteoporotic bone cements, a dual-adhesive bone cement is developed, which can form chemical bonds and physical adsorption with the bone tissue (Fig. 2A). This enhances the bone–cement interfacial adhesion strength and improves the degree of bone–cement bonding, facilitating better restoration of the bone microenvironment.

Herein, the bone adhesion performance of the antiosteoporotic bone cements was directly validated via bone fracture bonding experiments, as shown in Fig. 2B(i). The bone cement can be smoothly injected and adapt to the irregular shape of the fractured bone tissue, indicating the good flowability of the uncured bone cement, which can effectively fill irregular fractures. After curing, the bone cement strongly bonds with the bone tissue, reconnecting fractured bones. A further examination of the stability of the repaired bone tissue reveals that the repaired bone tissue can withstand the pressure of a standard 100-g weight without cracking or deformation under the action of the bone cement, indicating that the originally defective or failed bone tissue can regain its normal shape and mechanical support under the adhesive action of the bone cement (Fig. 2B(ii)). Subsequently, the bonded bone tissue was placed in flowing water (water pressure = 150–200 kPa). Impressively, the bone tissue exhibited strong adhesion under an intense water flow, indicating that the antiosteoporotic bone cements maintains good resistance to dispersion after bonding with the bone tissue (Fig. 2B(iii)). Furthermore, we subjected the bonded bone tissues to consecutive rinsing and subsequently dried and weighed the residual bone cement at predetermined time intervals to determine the residual mass ratio. As depicted in Fig. S13 (Supporting Information), the antiosteoporotic bone cements bonded to the bone tissues demonstrated favorable impact resistance within 24 h.

To comprehensively evaluate the bone adhesion performance of the antiosteoporotic bone cements, bone lap shear tests were performed to examine the lap-shear strength (Fig. 2C). First, the bone cement was injected into the test area on one bone slice; then, another bone slice was overlaid, gently pressed for 10 s, and tested after 15 min when the bone cement was fully cured. The results (Fig. 2D) show that with an increase in the mass fraction of ALN and excess LDI, the adhesive failure force gradually increases and failure displacement also increases. The adhesive failure force of A_4 is 153 N, higher than that of A_0 (76 N), confirming that the antiosteoporotic bone cement not only forms polyurea with the amino groups of the bone tissue using LDI but also physically binds with the abundant calcium ions on the bone tissue surface using ALN. The combined action of these two adhesion mechanisms achieves strong bonding to the bone tissue. The increasing failure displacement indicates that the introduction of ALN physically crosslinks the independent polymer and inorganic networks in the bone cement. This dynamic reversible electrostatic complexation during loading and unloading processes results in fracture and recombination, which helps dissipate external energy during adhesion and enhances the toughness of the antiosteoporotic bone cements, resulting in a ~100 % increase in failure displacement. The calculated shear strength of the antiosteoporotic bone cements exhibits a similar trend (Fig. 2E), indicating that throughout the bonding process, the dual-adhesive antiosteoporotic bone cements tightly bonds to the bone tissue and maintains volume stability by dissipating mechanical energy, demonstrating the strong interface adhesion strength and cohesive strength of the bone cements. To simulate the moist physiological environment, bone tissue was first immersed in PBS (pH = 7.4) and used without drying. After the cement cured, the adhesion area was kept moist condition by using PBS. As shown in Fig. S14 (Supporting Information), the antiosteoporotic bone cements maintain a certain level of adhesive strength even with prolonged exposure to a moist environment. Additionally, as the ALN content increases, the reduction in adhesive strength becomes less pronounced. This finding confirms that the dual adhesion mechanism effectively mitigates the impact of the moist environment on the adhesive performance of the antiosteoporotic bone cements. In vitro degradation experiments (Fig. S15 (Supporting Information)) further confirmed that the antiosteoporotic bone cements can remain stable over an extended period, providing mechanical support and maintaining strong adhesive properties. Because calcium ions are not present on the surface of the skin, bone–skin adhesion experiments were performed to further verify the dual-adhesive mechanism of the bone cement. As shown in Fig. 2F, bone–skin peel tests were performed to assess bone adhesion to the skin tissue. Fig. 2G and **H** shows that as the contents of ALN and excess LDI increase, the increase in interface toughness significantly increases. However, there is no significant difference in the interface toughness among the various antiosteoporotic bone cements. This is because ALN in the bone cement system is mainly attracted to the inorganic components in the system, which competitively react with LDI to a lesser extent, resulting in a smaller increase in interface toughness. This is because fewer LDI react with the amino groups on the skin surface, thereby leading to a smaller increase in interface toughness.

3.4. Antiosteoporotic bone cements regulate the acidic bone microenvironment and inhibits the in vitro differentiation of osteoclasts

The excessive activity of osteoclasts, leading to an imbalance in bone homeostasis, is the primary cause of osteoporosis, and the acidic microenvironment generated by overactive osteoclasts is a prominent feature of the osteoporotic bone tissue microenvironment [59–61]. In response to the overdifferentiated osteoclasts and uncontrolled acidic microenvironment in osteoporotic microenvironments, the antiosteoporotic bone cements releases ALN upon close integration with the bone tissue to suppress the hyperdifferentiated osteoclasts and utilizes the buffering capacity of calcium phosphate to regulate the uncontrolled acidic microenvironment, thereby improving the overall osteoporotic bone microenvironment (Fig. 3A). The biocompatibility of the antiosteoporotic bone cements were initially evaluated according to the relevant standards (ISO 10993–5:2009). As shown in Fig. S16 (Supporting Information), the cell viability of A_0–A_3 is ~90 %, exceeding the standard requirement of 70 %, thus meeting the standard. However, the cell viability of A_4 is significantly lower than 70 %, indicating its potential cytotoxicity and unsuitability for clinical use. Similarly, co-culture experiments with antiosteoporotic bone cements and bone marrow-derived macrophages cells confirmed the biocompatibility and biosafety of the cement (Fig. S17, Supporting Information). Furthermore, after implanting the antiosteoporotic bone cements into the femoral defects of rats for 1, 2, 3, 4, and 5 days, histological analysis of the rats' major organs and bone tissues indicated that the antiosteoporotic bone cements did not induce toxicity in the short term (Figs. S18 and S19, Supporting Information). Therefore, A_0–A_3 were used for subsequent experiments.

The antiosteoporotic bone cements achieve the overall regulation of the osteoporotic bone microenvironment using the cytotoxic effect of ALN on osteoclasts and the buffering effect of calcium phosphate. Therefore, evaluating the long-term release kinetics of ALN and buffering effect of the antiosteoporotic bone cements is necessary. As shown in Fig. 3B, the release behavior of ALN is evaluated as a relative burst within the first 24 h of testing, followed by sustained and sequential release within 40 days, with the release reaching ~50 % at 50 days, indicating that ALN still maintains a dynamic network in the antiosteoporotic bone cements. Fig. 3C shows the pH-regulation capability of the antiosteoporotic bone cements in a phosphate-buffered saline

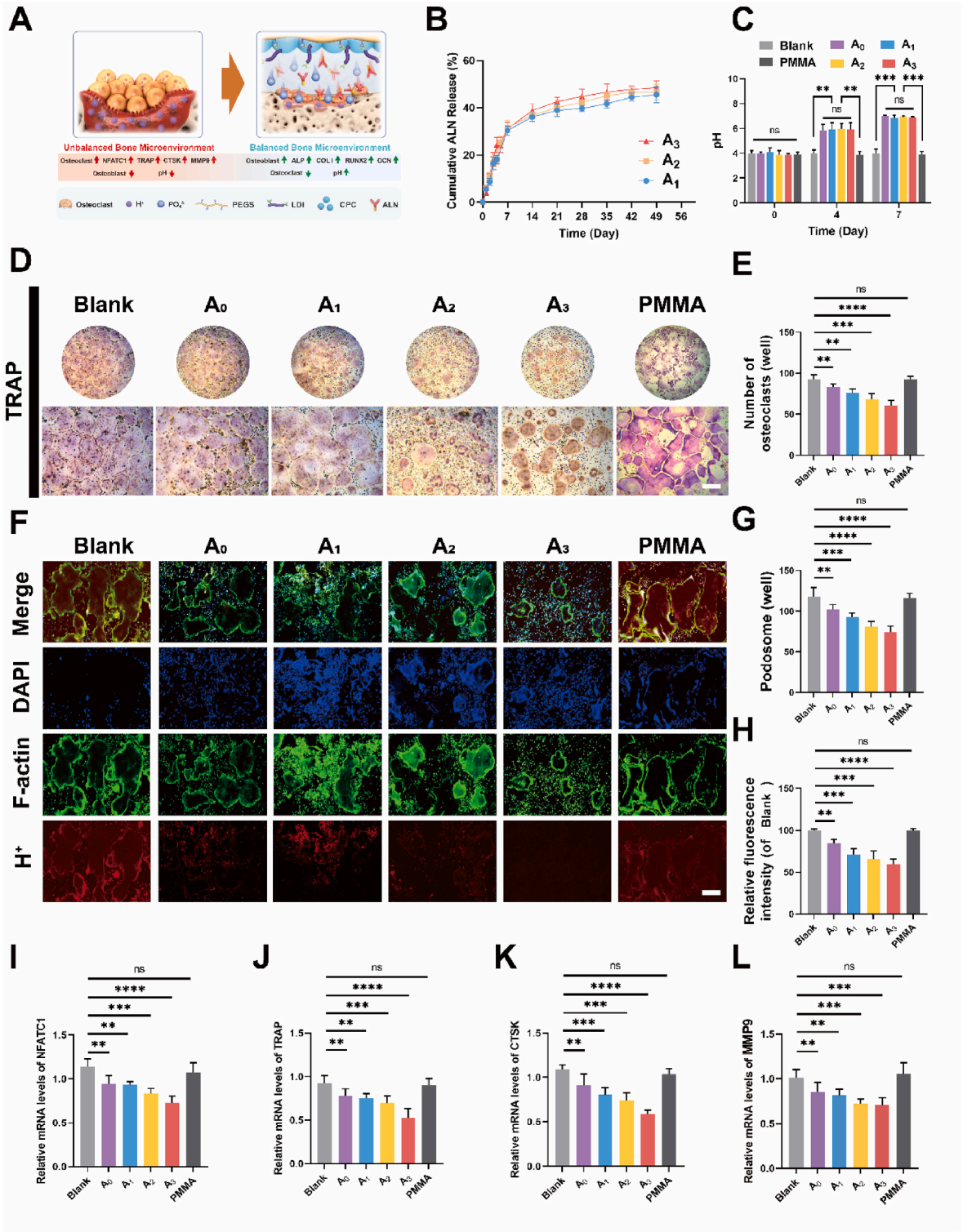

Fig. 3. Antiosteoporotic bone cements regulate the acidic bone microenvironment and inhibit the in vitro differentiation of osteoclasts. A) Schematic representation of the regulation of acidic bone microenvironment and effect on osteoclasts of the antiosteoporotic bone cement. B) ALN release kinetics from the antiosteoporotic bone cements in PBS solution. (n = 4; mean ± SD). C) The buffering effect of the antiosteoporotic bone cements in PBS solution. (n = 4; mean ± SD). D) TRAP staining was performed to detect osteoclast formation under the treatment of the antiosteoporotic bone cements extracted solutions. Scale bar: 400 μm. E) The count of TRAP-positive cells were statistically analyzed to evaluate the function of the antiosteoporotic bone cements. F) F-actin fluorescence and pH probe staining were conducted to evaluate the effects of the antiosteoporotic bone cements on the osteoclasts function (the blue represented the nucleolus, the green represented the actin cytoskeleton, and the red represented the H^+). Scale bar: 200 μm. G) The count of podosome in each group were analyzed to demonstrate the function of the antiosteoporotic bone cements. H) Quantitative intensities of OCs labeled with pH probes after treatment with the antiosteoporotic bone cements. Real-time PCR analysis of osteoclast marker genes I) NFATC1, J) TRAP, K) CTSK, and L) MMP9 in BMMs under the treatment of the antiosteoporotic bone cements for 5 days. (mean ± SD; n = 4; *$p < 0.05$; **$p < 0.01$, ***$p < 0.001$; ****$p < 0.0001$).

(PBS; pH = 4.0). PMMA and the blank without any added material lack pH-regulation capability. The antiosteoporotic bone cements can improve the pH of the system from an acidic environment (pH 4.0) to a weakly acidic environment (pH 6.0) within 4 days and complete the regulation of the acidic environment within 7 days, neutralizing the bone microenvironment. To further evaluate the influence of the antiosteoporotic bone cements on osteoclast survival and their regulatory effects on the bone microenvironment, TRAP staining, podosome formation, cellular environment pH detection, and osteoclast-specific marker gene expression were performed. TRAP is a marker of the osteoclast phenotype synthesized by osteoclast-like cells [62]. After coculturing the antiosteoporotic bone cements with osteoclasts for 5 days, the status of osteoclasts was measured, and the results are shown in Fig. 3D. Compared with the blank, PMMA has almost no effect on osteoclast formation but A_0 without ALN has a certain inhibitory effect on osteoclast formation, confirming that the bone cement inhibits osteoclast formation by regulating the acidic microenvironment. Furthermore, among A_1–A_3, the reduction in osteoclast formation is most significant in A_3. Similar conclusions can be drawn from the quantitative analysis of the number of osteoclasts in the well plate (Fig. 3E). Immunofluorescence staining was used to observe the status of osteoclasts, which reveals that cells in the blank and PMMA are multinucleated with continuous actin rings but the antiosteoporotic bone cements significantly inhibits the formation of actin rings in multinucleated osteoclasts (Fig. 3F). Podosome formation is a key structure of mature osteoclasts and a crucial indicator of bone resorption activity. Quantitative analysis of the number of podosomes in osteoclasts from each group shows a significant decrease in the periphery of osteoclasts after treatment with the antiosteoporotic bone cements (Fig. 3G). Mature osteoclasts secrete proton and lysosomal enzymes into the bone resorption pit to lower the local pH and induce bone matrix degradation, forming Howship's lacunae [63,64]. Therefore, pH-sensing chemical probes such as AIE™ pH probes can be used to analyze the pH of the microenvironment. The fluorescence of pH-sensing chemical probes changes from red to blue as pH increases. As shown in Fig. 3F, a large number of mature osteoclasts in the blank and PMMA exhibit intense red fluorescence. Under the action of the antiosteoporotic bone cements, the fluorescence intensities of A_0–A_3 gradually decrease (Fig. 3H). These results confirm that the antiosteoporotic bone cements can achieve close adhesion to bone tissue while effectively promoting the apoptosis of overactive osteoclasts through the controlled release of ALN. This process reduces the production of H^+ typically associated with overactivated osteoclasts. Furthermore, the CPC component within the bone cement provides a phosphate buffering effect, which helps neutralize the excess H^+ in the bone microenvironment. Through the dual mechanisms of directly modulating the acidic microenvironment and inducing osteoclast apoptosis, the antiosteoporotic bone cement mitigates the pathological acidification characteristic of osteoporotic bone, thereby facilitating the restoration of a healthier bone microenvironment. Measurements of the pH of the osteoclast culture medium after treatment with the antiosteoporotic bone cements yield results consistent with the TRAP staining (Fig. S20, Supporting Information). Additionally, the expression of osteoclast-specific marker genes, including CTSK, TRAP, nuclear factor of activated T-cells cytoplasmic 1 (NFATC1), and matrix metalloproteinase 9 (MMP9), was evaluated via the quantitative reverse transcription-polymerase chain reaction (qRT-PCR). CTSK is a well-known osteoclast inducer and an important marker of osteoclast activation [65]. NFATC1 is a key transcription factor regulating osteoclast formation and differentiation, which controls the expression levels of CTSK and TRAP [66]. Cells treated with the antiosteoporotic bone cements show significantly lower mRNA levels of all four markers compared to the blank and PMMA, with the lowest levels observed in cells treated with A_3. These results indicate that the antiosteoporotic bone cements inhibit osteoclast differentiation and cellular function by suppressing the expression of osteoclast-related genes, including CTSK, TRAP, NFATC1, and MMP9.

3.5. Antiosteoporotic bone cements promote osteogenic differentiation and mineralization of BMSCs in vitro

In the treatment of osteoporosis, aside from suppressing overactive osteoclasts, promoting proliferation and inducing the osteogenic differentiation of bone marrow mesenchymal stem cells (BMSCs) plays a crucial role [67]. The antiosteoporotic bone cements facilitate BMSC proliferation and directs differentiation toward osteoblasts by releasing Ca^{2+} (Fig. 4A). Therefore, the proliferative effects of BMSCs treated with different bone cements were evaluated using the cell counting kit-8 (CCK-8) method, as shown in Fig. S21 (Supporting Information). On the 4th day of culturing, compared to the blank and PMMA, the antiosteoporotic bone cements promote BMSC proliferation. On the 7th day, the antiosteoporotic bone cements exhibit significantly enhanced proliferation and no significant differences are observed among different bone cements, implying that the addition of ALN and LDI does not affect BMSC proliferation. A further assessment of the long-term release kinetics of Ca^{2+} from the antiosteoporotic bone cements show similar release behaviors among different bone cements (Fig. 4B). Furthermore, the antiosteoporotic bone cements exhibit the capacity for sustained calcium ion release over extended periods, even within a bone microenvironment that closely mimics the conditions of osteoporosis (Fig. S22 (Supporting Information). This stability in calcium ion release underscores the cement's efficacy in maintaining its functional performance and providing continuous support for bone regeneration in a pathological setting. The impact of the antiosteoporotic bone cements on osteogenic differentiation was studied via alkaline phosphatase (ALP) staining, alizarin red S (ARS) staining, and analysis of osteogenic gene expression correlations. As shown in Fig. 4C, on the 14th day of culturing, BMSCs treated with the antiosteoporotic bone cements exhibit stronger ALP staining intensity than cells treated with the blank and PMMA. Further quantitative analysis reveals that BMSCs treated with the antiosteoporotic bone cements exhibit higher ALP activity than cells treated with the blank and PMMA (Fig. 4D). This is attributed to the sustained release of Ca^{2+} from the antiosteoporotic bone cements, which promotes the differentiation of stem cells toward osteoblasts. ARS staining and quantitative analysis also show consistent results with ALP staining analysis, indicating the favorable mineralization activity of the antiosteoporotic bone cements (Fig. 4E and F). Additionally, the qRT-PCR was employed to further assess the expression levels of ALP, type I collagen (COL I), Runt-related transcription factor 2 (RUNX 2), and osteocalcin (OCN) in BMSCs (Fig. 4G–J). Compared to the blank and PMMA, the antiosteoporotic bone cements significantly upregulate ALP, RUNX 2, OCN, and COL I under the influence of Ca^{2+}, implying its promotional effect on osteogenic differentiation.

3.6. In vivo bone remodeling effects of the antiosteoporotic bone cement on bone defect regeneration in osteoporotic rats

As the composition of the antiosteoporotic bone cements varied, changes in mechanical strength, bone tissue adhesion, and osteoclast inhibition capability are observed, as shown in Fig. 5A. Among A_0, A_1, A_2 and A_3, A_3 exhibits optimal mechanical, bone adhesion, and bone microenvironment repair performance. Consequently, A_3 was used as the experimental group for subsequent experiments.

To further investigate the specific roles and underlying mechanisms of the antiosteoporotic bone cements in bone reconstruction and homeostasis in osteoporotic bone defects, an osteoporotic bone defect model was established in ovariectomy (OVX) rats (Fig. 5B). Clinical-grade PMMA and CPC were chosen as positive groups, and materials were injected into OVX rats, followed by the assessment of bone defect repair 6 and 12 weeks postimplantation. New bone formation was observed via micro-computed tomography (micro-CT), and three-dimensional (3D) reconstructed images were visualized (Fig. 5C). The defects in the blank remain as large voids 6 weeks postimplantation, indicating the difficulty in spontaneous femoral healing in osteoporotic

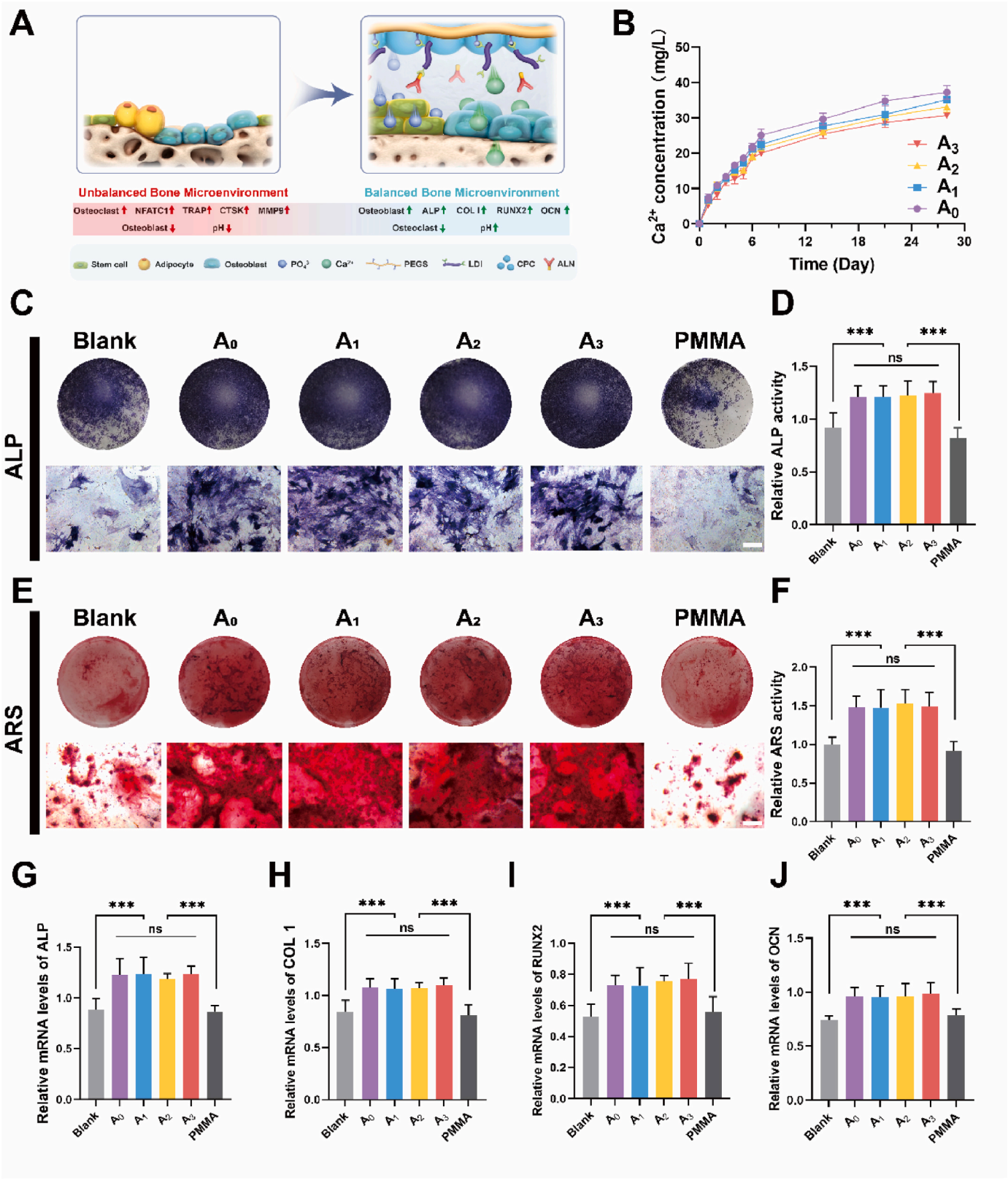

Fig. 4. Antiosteoporotic bone cements promote osteogenic differentiation and mineralization of BMSCs in vitro. A) Schematic representation of the promotion of osteogenic differentiation of stem cells by the antiosteoporotic bone cements. B) Ca^{2+} ions release curve of the antiosteoporotic bone cements over 28 days. C) ALP staining of BMSCs cultured on the antiosteoporotic bone cements at day 14. Scale bar: 200 μm. D) Quantification of ALP activity on day 14. E) ARS staining of BMSCs cultured on the antiosteoporotic bone cements at day 21. Scale bar: 200 μm. F) Quantification of ARS activity on day 21. G) ALP, H) COL I, I) RUNX2, and J) OCN in BMSCs under the treatment of the antiosteoporotic bone cements for 7 days (mean ± SD; n = 4; ***$p < 0.001$).

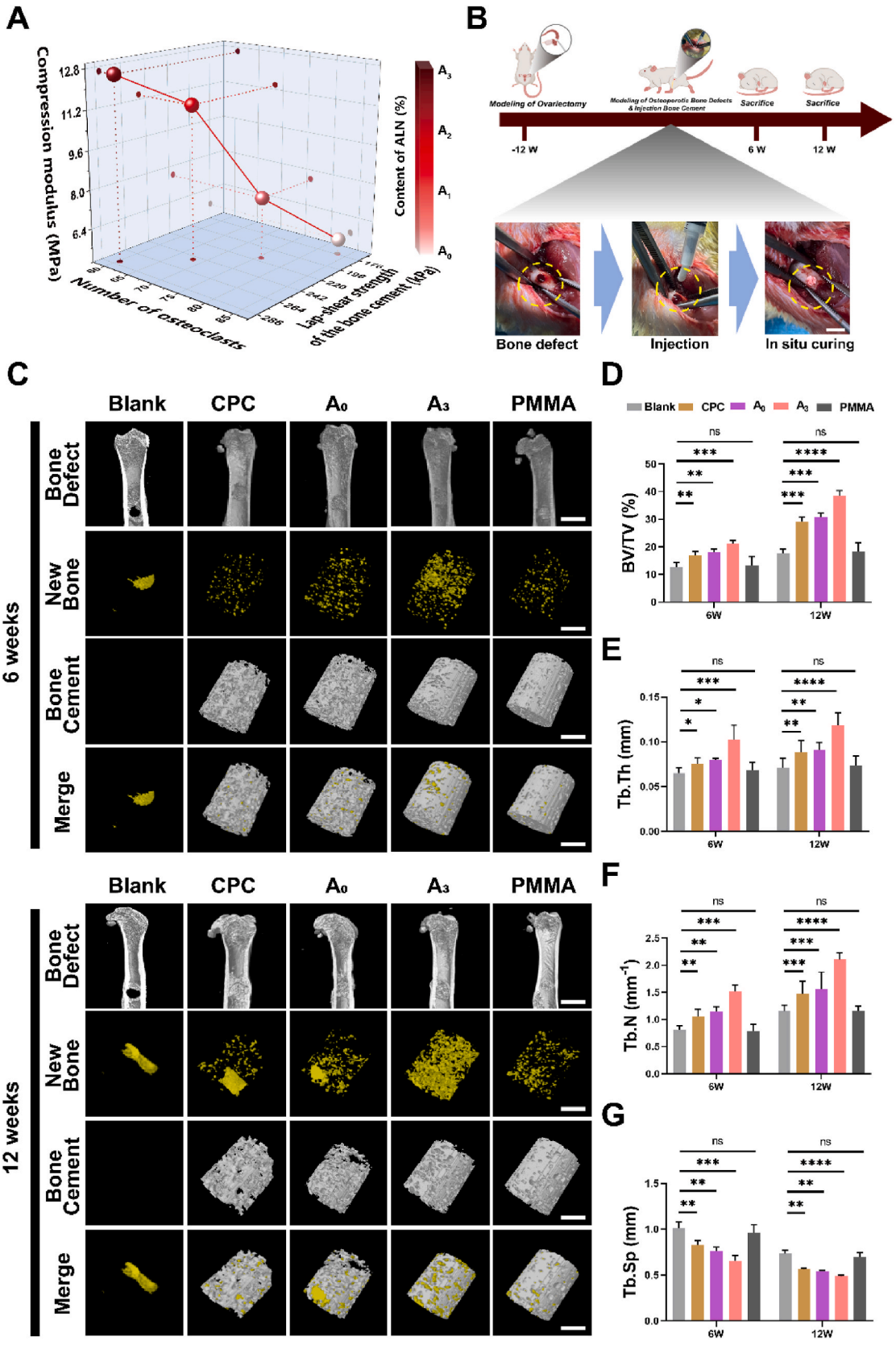

Fig. 5. In vivo bone remodeling effects of the antiosteoporotic bone cement on bone defect regeneration in osteoporotic rats. A) Relationship between compressive strength, lap-shear strength and osteoclasts quantity of the antiosteoporotic bone cement with different formulations. B) Schematic representation and digital pictures of model and treatment of osteoporotic bone defects. The yellow circle marks the defect in the femur. Scale bar: 4 mm. C) Reconstructed micro-CT images of the femur in OVX rats treated with the antiosteoporotic bone cement for 6 and 12 weeks. Scale bar in the Bone Defect: 4 mm. Scale bar in the New Bone, Bone Cement and Merge: 1 mm. Quantification of D) bone volume fraction (BV/TV; %), E) trabecular thickness (Tb.Th; mm), F) trabecular number (Tb. N; mm^{-1}) and G) trabecular separation (Tb.Sp; mm) derived from micro-CT at 6 and 12 weeks. (mean ± SD; n = 5; *$p < 0.05$; **$p < 0.01$; ***$p < 0.001$; ****$p < 0.0001$).

rats. PMMA exhibits effects similar to the blank owing to its strong biological inertness, and the interfaces between PMMA and surrounding bone tissues remain independent, demonstrating the absence of the integration between PMMA and bone tissues. The repair levels of CPC and A_0 are relatively similar, showing good integration with bone tissues. Leveraging its excellent bone adhesion and bone microenvironment repair capabilities, A_3 exhibits the best performance in bone defect repair. Additionally, as observed in Fig. 5C, after 6 and 12 weeks of repairing the bone defect with antiosteoporotic bone cement, a portion of the cement remains undegraded within the defect site. The

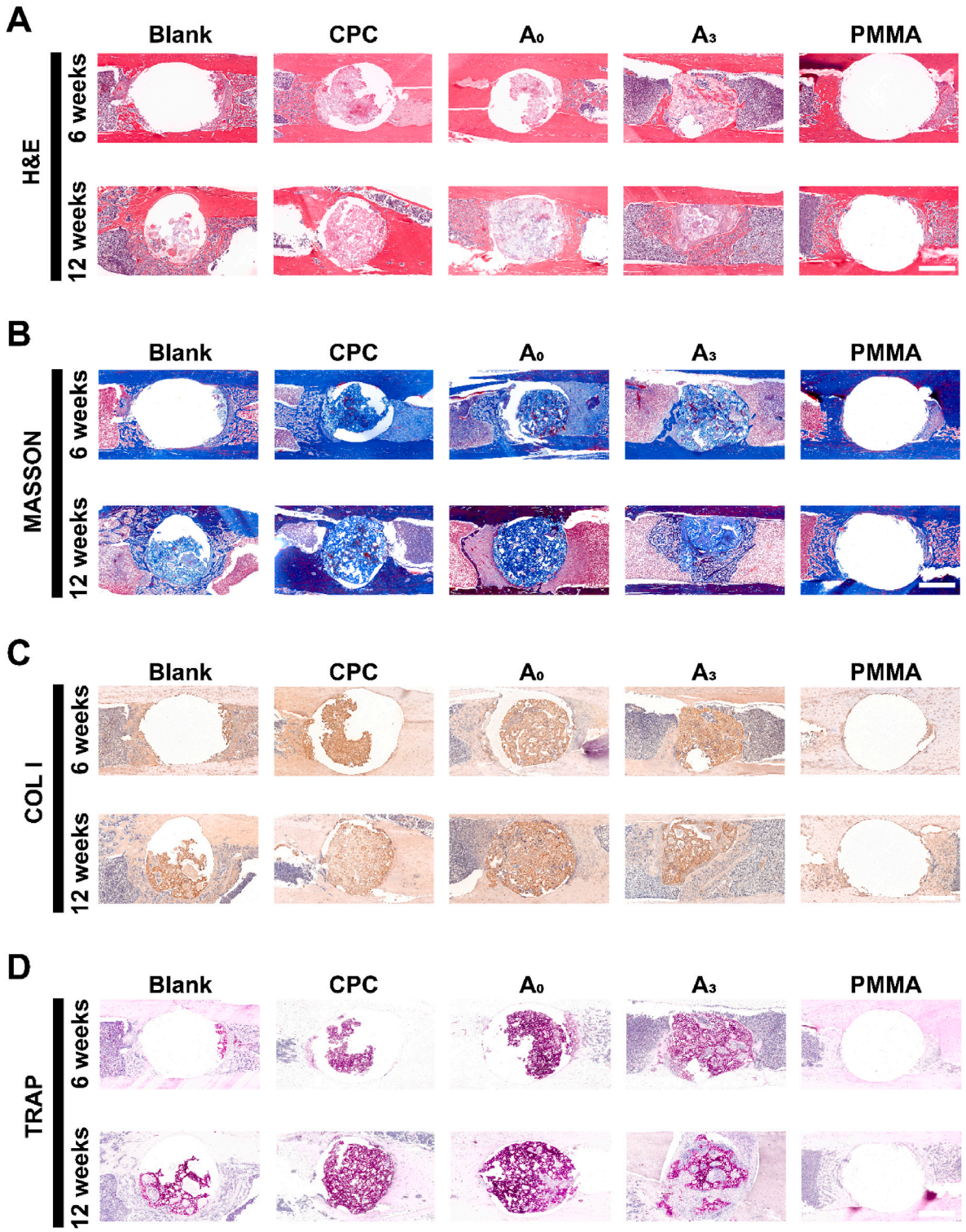

Fig. 6. Histological observation of new bone formation in osteoporosis rats after treatment of the antiosteoporotic bone cement. A) Representative images of hematoxylin and eosin (H&E) staining of the histopathological bone tissue treated with the antiosteoporotic bone cement. B) Representative images of masson trichrome (Masson) histochemical stain of the newly-formed bone in the defect treated by the antiosteoporotic bone cement. C) Representative images of collagen I (COL I) staining of the histopathological bone tissue treated by the antiosteoporotic bone cement. D) Representative images of Tartrate-resistant acid phosphatase (TRAP) staining of the histopathological bone tissue treated by the antiosteoporotic bone cement. Scale bar: 1 mm.

residual bone cement is primarily composed of CPC, which not only maintains the structural integrity of the defect site but also provides an environment conducive to cellular growth [68–70]. Furthermore, it continuously releases calcium ions, which promote the differentiation of osteoblasts and accelerate bone formation [56]. Microstructural parameters of the newly formed bone within the defects at 12 weeks confirm these results (Fig. 5D–G). The bone volume fraction (BV/TV) of A_3 (38.53 ± 0.81 %) is greater than those of CPC, A_0, and PMMA (which are 29.24 ± 0.69 %, 30.73 ± 1.45 %, and 18.24 ± 1.43 % respectively) at 12 weeks. Notably, the trabecular thickness (Tb. Th, Fig. 5E) and trabecular number (Tb. N, Fig. 5F) exhibit similar trends. However, trabecular separation (Tb. Sp, Fig. 5G) is minimal in A_3, indicating that the regenerated bone tissue in A_3 is denser than other groups. These results suggest that the dual-network bone-adhesive bone cement can significantly prevent bone loss in osteoporotic bone defects and promote bone healing.

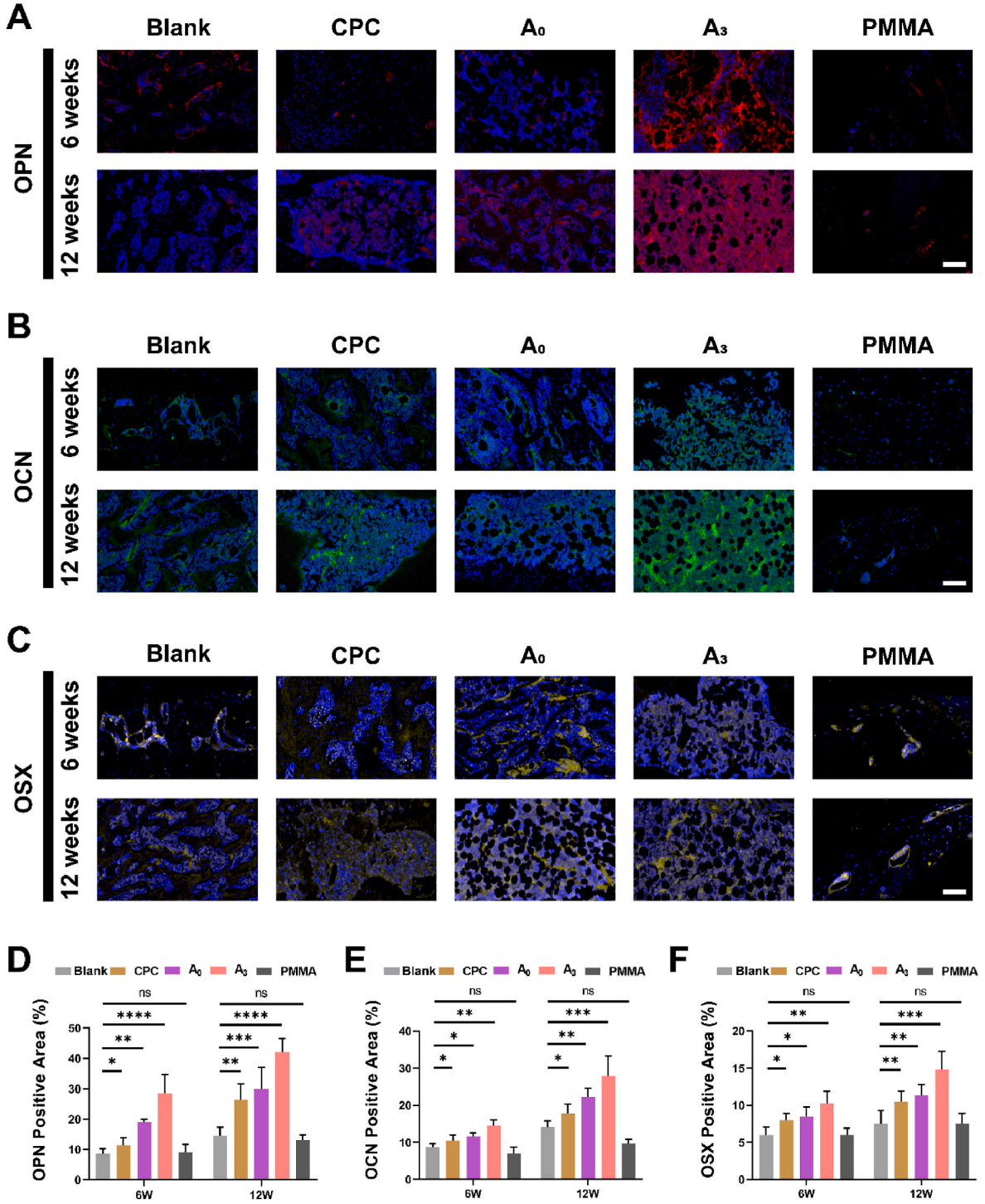

Fig. 7. Immunohistochemical staining images of bone defects after treatment of the antiosteoporotic bone cement. Immunofluorescence of A) osteopontin (OPN, red), B) osteocalcin (OCN, green) and osterix (OSX, yellow) in the bone defects 6 and 12 weeks after surgery. Quantifications of D) OPN, E) OCN and F) OSX positive area in bone defects. Scale bar: 100 μm. (mean ± SD; n = 5; $^{*}p < 0.05$; $^{**}p < 0.01$; $^{***}p < 0.001$; $^{****}p < 0.0001$).

3.7. Histological observation of new bone formation in osteoporosis rats after treatment of the antiosteoporotic bone cement

To further evaluate the efficacy of the antiosteoporotic bone cement in promoting in vivo bone regeneration, bone sections were stained with hematoxylin and eosin (H&E), Masson, and TRAP. Representative microphotographs of H&E staining are shown in Fig. 6A. In defects treated with A_3, there is evident recruitment of natural cells and substantial formation of thick granulation tissues composed of inflammatory cells and fibroblasts derived from collagen, showing significant histological changes and improvement in the bone tissue structure compared to the blank. Masson trichrome staining (Fig. 6B) was further used to examine the formation of bone tissues within defects repaired with the antiosteoporotic bone cement 6 and 12 weeks postrepair. Representative histological images show that more new bones grow inward through the pores of the bone cement in CPC, A_0, and A_3, with A_3 showing a greater ingrowth volume than the other two groups. The staining results of COL I in Fig. 6C confirm the bone repair efficacy of A_3. However, the blank and PMMA-treated groups show little bone tissue growth at defect margins and thinner soft tissues connecting defects. Remarkably, a comprehensive analysis of H&E and Masson staining indicates that compared to biologically inert PMMA, other groups of materials exhibit varying degrees of integration with bone tissues, among which A_3 exhibits the best fusion with the newly formed bone tissue 12 weeks postrepair, consistent with the results of micro-CT scans. These results prove that the antiosteoporotic bone cement achieves strong integration with bone tissues via its excellent bone adhesion and effective bone microenvironment regulation capabilities. Additionally, TRAP staining was employed to evaluate the effect of the antiosteoporotic bone cement on osteoclast formation. As shown in Fig. 6D, the number of osteoclasts near the edges of bone defects in the blank or PMMA-treated groups is significantly higher than that in other groups. In the late stage of bone tissue repair, smaller TRAP-positive areas are observed in A_3, indicating the inhibition of osteoclasts within osteoporotic bone tissues. The expressions of osteogenic factors (i.e., osteopontin (OPN), osteocalcin (OCN) and osterix (OSX)) in osteoporotic bone defect after the antiosteoporotic bone cement treatment were further investigated by immunohistochemical (IHC) staining. The positive expressions of OPN, OCN and OSX were obviously identified in the cells growing into A_3, while the expressions in A_0, CPC and other groups were weak (Fig. 7A–C). From the quantitative analysis (Fig. 7D–F), it could be observed that the cells in A_3 had significantly higher expressions of OPN, OCN and OSX than those in A_0, CPC and other groups, and these expressions in PMMA were the lowest. These results all indicate that PEGS/CPC@ALN bone cement have good osteogenesis ability and osteoporotic bone microenvironment modulatory capacity in vivo. Finally, pathological sections of major organs further demonstrate no apparent pathological damage to the heart, liver, spleen, lungs, or kidneys (Fig. S23, Supporting Information).

4. Conclusion

Disrupted bone remodeling caused by excessive osteoclast activity is the primary cause of osteoporosis. Herein, a dual-network, injectable, and bone-adhesive bone cement was developed using clinically approved materials to modulate the osteoporotic bone microenvironment for effective bone regeneration. Our findings demonstrate that ALN connects the PEGS organic network crosslinked by LDI and the CPC-formed inorganic network via its amino and bisphosphonate groups. This dual-network integration significantly enhances the mechanical properties of the antiosteoporosis bone cements, contributing to its stability at the implantation site. Furthermore, after ALN is linked with LDI, it can select amino groups on the surface of bone tissue as adhesion sites, tightly connecting with the bone tissue. This enhances the binding degree between the antiosteoporosis bone cements and the bone tissue, allowing the cement to function more effectively. Additionally, ALN can be released through the natural degradation of the material, inhibiting the excessively active osteoclasts in the osteoporotic bone microenvironment and restoring bone homeostasis. By introducing the ALN, the mechanical properties, bone adhesion performance, and pathological osteoporotic bone microenvironment regulation capabilities of the antiosteoporosis bone cements are all improved. This demonstrates the synergistic effect between the drug and the material in our study. The antiosteoporotic bone cement possesses dual interconnected networks and effectively regulates osteoclasts and their microenvironment via drug release and by leveraging the advantages of the antiosteoporotic bone cement system. Moreover, it stimulates osteogenesis and seamlessly integrates with the bone tissue, achieving a harmonious balance between osteoblasts and osteoclasts while promoting the in vivo regeneration of osteoporotic bones. The outstanding performance of the antiosteoporotic bone cement makes it a promising candidate among minimally invasive materials for treating osteoporosis, offering a highly translational strategy for addressing degenerative bone diseases. However, to ensure successful clinical application, challenges such as manufacturing scalability, regulatory approval and accessibility must be addressed, making it essential to overcome these hurdles to advance the clinical utility of the antiosteoporotic bone cement.

Ethics approval and consent to participate

All procedures followed the National Institute of Health Guide for the Care and Use of Laboratory Animals and were approved by the Shanghai Rat & Mouse Biotech., LTD (approved number: 20230301(7) and 20240630(09)).

CRediT authorship contribution statement

Lingfei Zhao: Writing – review & editing, Writing – original draft, Project administration, Methodology, Investigation, Formal analysis, Data curation. **Chenyu Liu:** Writing – original draft, Visualization, Data curation. **Xing Chen:** Methodology, Data curation. **Zirui He:** Writing – review & editing. **Shuiquan Zhang:** Writing – review & editing, Data curation. **Anan Zhang:** Writing – review & editing. **Shuaimin Tang:** Writing – review & editing. **Zihan Wu:** Conceptualization. **Changsheng Liu:** Funding acquisition, Conceptualization. **Yuan Yuan:** Project administration, Funding acquisition, Conceptualization.

Declaration of competing interest

Zihan Wu is currently employed by Shanghai Rebone Biomaterials Co., Ltd. The authors declare no conflict of interest.

Acknowledgements

The authors wish to express their gratitude to the financial support from National Key Research and Development Program of China (No.2022YFB3804300) and (No.2022YFC2405702) , Program of Shanghai Academic/Technology Research Leader (22XD1433900), Frontiers Science Center for Materiobiology and Dynamic Chemistry (No.JKVD1211002), and Chinese Academy of Sciences-WEGO Research and Development Program ([2023]005), and the National Natural Science Foundation of China (No.32271401)

Appendix B. Supplementary data

Supplementary data to this article can be found online at https://doi.org/10.1016/j.bioactmat.2024.09.032.

References

[1] J.E. Compston, M.R. McClung, W.D. Leslie, Osteoporosis, Lancet 393 (10169) (2019) 364–376.

[2] T.D. Rachner, S. Khosla, L.C. Hofbauer, Osteoporosis: now and the future, Lancet 377 (9773) (2011) 1276–1287.
[3] L. Zheng, Z. Zhuang, Y. Li, T. Shi, K. Fu, W. Yan, L. Zhang, P. Wang, L. Li, Q. Jiang, Bone targeting antioxidative nano-iron oxide for treating postmenopausal osteoporosis, Bioact. Mater. 14 (2022) 250–261.
[4] Y. Cui, Y. Guo, L. Kong, J. Shi, P. Liu, R. Li, Y. Geng, W. Gao, Z. Zhang, D. Fu, A bone-targeted engineered exosome platform delivering siRNA to treat osteoporosis, Bioact. Mater. 10 (2022) 207–221.
[5] L.G. Raisz, Pathogenesis of osteoporosis: concepts, conflicts, and prospects, J. Clin. Invest. 115 (12) (2005) 3318–3325.
[6] R.L. Jilka, G. Hangoc, G. Girasole, G. Passeri, D.C. Williams, J.S. Abrams, B. Boyce, H. Broxmeyer, S.C. Manolagas, Increased osteoclast development after estrogen loss mediation by INTERLEUKIN-6, Science 257 (5066) (1992) 88–91.
[7] W. Zhang, K.T. Tao, J. Lin, P. Liu, Z. Guan, J. Deng, D. Wang, H. Zeng, The role of m6A in osteoporosis and the differentiation of mesenchymal stem cells into osteoblasts and adipocytes, Curr. Stem Cell Res. Ther. 18 (3) (2023) 339–346.
[8] W.J. Boyle, W.S. Simonet, D.L. Lacey, Osteoclast differentiation and activation, Nature 423 (2003) 337–342.
[9] H. Fu, L. Wang, Q. Bao, D. Ni, P. Hu, J. Shi, Acid neutralization and immune regulation by calcium-aluminum-layered double hydroxide for osteoporosis reversion, J. Am. Chem. Soc. 144 (20) (2022) 8987–8999.
[10] Z. Li, H. Wang, K. Zhang, B. Yang, X. Xie, Z. Yang, L. Kong, P. Shi, Y. Zhang, Y. P. Ho, Z.Y. Zhang, G. Li, L. Bian, Bisphosphonate-based hydrogel mediates biomimetic negative feedback regulation of osteoclastic activity to promote bone regeneration, Bioact. Mater. 13 (2022) 9–22.
[11] S. Khosla, L.C. Hofbauer, Osteoporosis treatment: recent developments and ongoing challenges, Lancet Diabetes Endocrinol. 5 (11) (2017) 898–907.
[12] X. Feng, J.M. McDonald, Disorders of bone remodeling, Annu. Rev. Pathol. 6 (1) (2011) 121–145.
[13] L. Che, Y. Wang, D. Sha, G. Li, Z. Wei, C. Liu, Y. Yuan, D. Song, A biomimetic and bioactive scaffold with intelligently pulsatile teriparatide delivery for local and systemic osteoporosis regeneration, Bioact. Mater. 19 (2023) 75–87.
[14] E. Hsu, M. Nanes, Advances in treatment of glucocorticoid-induced osteoporosis, Curr. Opin. Endocrinol. Diabetes Obes. 24 (6) (2017) 411–417.
[15] C.N. Cornell, Internal fracture fixation in patients with osteoporosis, J. Am. Acad. Orthop. Surg. 11 (2) (2003) 109–119.
[16] B. Mjöberg, H. Pettersson, R. Rosenqvist, A. Rydholm, Bone cement, thermal injury and the radiolucent zone, Acta Orthop. Scand. 55 (6) (1984) 597–600.
[17] Z. Huan, J. Chang, Novel bioactive composite bone cements based on the β-tricalcium phosphate–monocalcium phosphate monohydrate composite cement system, Acta Biomater. 5 (4) (2009) 1253–1264.
[18] M.P. Ginebra, M. Espanol, E.B. Montufar, R.A. Perez, G. Mestres, New processing approaches in calcium phosphate cements and their applications in regenerative medicine, Acta Biomater. 6 (8) (2010) 2863–2873.
[19] S. Vieira, S. Vial, R.L. Reis, J.M. Oliveira, Nanoparticles for bone tissue engineering, Biotechnol. Prog. 33 (3) (2017) 590–611.
[20] X. Lin, Q. Wang, C. Gu, M. Li, K. Chen, P. Chen, Z. Tang, X. Liu, H. Pan, Z. Liu, R. Tang, S. Fan, Smart nanosacrificial layer on the bone surface prevents osteoporosis through acid-base neutralization regulated biocascade effects, J. Am. Chem. Soc. 142 (41) (2020) 17543–17556.
[21] Y. Niu, Y. Yang, Z. Yang, X. Wang, P. Zhang, L. Lv, Y. Liu, Y. Liu, Y. Zhou, Aptamer-immobilized bone-targeting nanoparticles in situ reduce sclerostin for osteoporosis treatment, Nano Today 45 (2022) 101529–101543.
[22] Y. Jiang, J. Li, X. Xue, Z. Yin, K. Xu, J. Su, Engineered extracellular vesicles for bone therapy, Nano Today 44 (2022) 101487–101510.
[23] D. Gundapaneni, T. Goswami, Thermal isotherms in PMMA and cell necrosis during total hip arthroplasty, J. Appl. Biomater. Funct. Mater. 12 (3) (2014) 193–202.
[24] Ferracini Bistolfi, Vernè Albanese, Miola, PMMA-based bone cements and the problem of joint arthroplasty infections: status and new perspectives, Materials 12 (23) (2019) 4002–4018.
[25] D.N. Chao Guo, Jia Liu, Xiaogang Bao, Guohua Xu, Application of biodegradable PLGA-PEG-PLGA/CPC composite bone cement in the treatment of osteoporosis, Coatings 11 (2021) 827–838.
[26] L. Chen, Y. Tang, K. Zhao, X. Zha, M. Wei, Q. Tan, Z. Wu, Sequential release of double drug (graded distribution) loaded gelatin microspheres/PMMA bone cement, J. Mater. Chem. B 9 (2) (2021) 508–522.
[27] A. Vezenkova, J. Locs, Sudoku of porous, injectable calcium phosphate cements – path to osteoinductivity, Bioact. Mater. 17 (2022) 109–124.
[28] Ö. Demir-Oğuz, A.R. Boccaccini, D. Loca, Injectable bone cements: what benefits the combination of calcium phosphates and bioactive glasses could bring? Bioact. Mater. 19 (2023) 217–236.
[29] Z. He, C. Sun, Y. Ma, X. Chen, Y. Wang, K. Chen, F. Xie, Y. Zhang, Y. Yuan, C. Liu, Rejuvenating aged bone repair through multihierarchy reactive oxygen species-regulated hydrogel, Adv. Mater. 36 (9) (2024) 2306552–2306567.
[30] A. Patel, A.K. Gaharwar, G. Iviglia, H. Zhang, S. Mukundan, S.M. Mihaila, D. Demarchi, A. Khademhosseini, Highly elastomeric poly(glycerol sebacate)-co-poly(ethylene glycol) amphiphilic block copolymers, Biomaterials 34 (16) (2013) 3970–3983.
[31] L. Sun, Y. Ma, H. Niu, Y. Liu, Y. Yuan, C. Liu, Recapitulation of in situ endochondral ossification using an injectable hypoxia-mimetic hydrogel, Adv. Funct. Mater. 31 (5) (2020) 2008515–2008534.
[32] Z. Wu, Z. Yang, D. Sha, Y. Ma, B.Y.S. Kim, W. Jiang, Y. Yuan, C. Liu, Injectable, viscoelastic hydrogel precisely regulates developmental tissue regeneration, Chem. Eng. J. 434 (15) (2022) 133860–133872.
[33] J.H. Lin, Bisphosphonates: a review of their pharmacokinetic properties, Bone 18 (2) (1996) 75–85.
[34] S.H. Tella, J.C. Gallagher, Prevention and treatment of postmenopausal osteoporosis, J. Steroid Biochem. Mol. Biol. 142 (2014) 155–170.
[35] R.A. Adler, G. El-Hajj Fuleihan, D.C. Bauer, P.M. Camacho, B.L. Clarke, G.A. Clines, J.E. Compston, M.T. Drake, B.J. Edwards, M.J. Favus, S.L. Greenspan, R. McKinney Jr., R.J. Pignolo, D.E. Sellmeyer, Managing osteoporosis in patients on long-term bisphosphonate treatment: report of a task force of the American society for bone and mineral research, J. Bone Miner. Res. 31 (1) (2015) 16–35.
[36] A.J. Roelofs, K. Thompson, S. Gordon, M.J. Rogers, Molecular mechanisms of action of bisphosphonates: current status, Clin. Cancer Res. 12 (20 Pt 2) (2006) 6222s–6230s.
[37] R.G. Russell, Z. Xia, J.E. Dunford, U. Oppermann, A. Kwaasi, P.A. Hulley, K. L. Kavanagh, J.T. Triffitt, M.W. Lundy, R.J. Phipps, B.L. Barnett, F.P. Coxon, M. J. Rogers, N.B. Watts, F.H. Ebetino, Bisphosphonates: an update on mechanisms of action and how these relate to clinical efficacy, Ann. N. Y. Acad. Sci. 1117 (2007) 209–257.
[38] M.J. Rogers, New insights into the molecular mechanisms of action of bisphosphonates, Curr. Pharmaceut. Des. 9 (32) (2003) 2643–2658.
[39] H. Wu, S. Huang, Y. Zhu, J. Li, X. Pang, Y. Tang, S. Li, P. Ji, S. Ding, W. Cheng, W. Li, Self-mineralizing dnazyme hydrogel as a multifaceted bone microenvironment amendment for promoting osteogenesis in osteoporosis, Adv. Funct. Mater. 33 (19) (2023) 2212669–2212684.
[40] S.-B. Woo, J.W. Hellstein, J.R. Kalmar, Systematic review: bisphosphonates and osteonecrosis of the jaws, Ann. Intern. Med. 144 (10) (2006) 753–761.
[41] K. Chen, Z. Wu, Y. Liu, Y. Yuan, C. Liu, Injectable double-crosslinked adhesive hydrogels with high mechanical resilience and effective energy dissipation for joint wound treatment, Adv. Funct. Mater. 32 (12) (2021) 2109687–2109703.
[42] C.I.A. van Houdt, P.R. Gabbai-Armelin, P.M. Lopez-Perez, D.J.O. Ulrich, J. A. Jansen, A.C.M. Renno, J. van den Beucken, Alendronate release from calcium phosphate cement for bone regeneration in osteoporotic conditions, Sci. Rep. 8 (1) (2018) 15398–15411.
[43] K.L. Lin, L.G. Xia, H.Y. Li, X.Q. Jiang, H.B. Pan, Y.J. Xu, W.W. Lu, Z.Y. Zhang, J. Chang, Enhanced osteoporotic bone regeneration by strontium-substituted calcium silicate bioactive ceramics, Biomaterials 34 (38) (2013) 10028–10042.
[44] Y. Zhao, H. Kang, X. Wu, P. Zhuang, R. Tu, T. Goto, F. Li, H. Dai, Multifunctional scaffold for osteoporotic pathophysiological microenvironment improvement and vascularized bone defect regeneration, Adv. Healthcare Mater. 12 (15) (2023) 2203099–2203116.
[45] K. Li, L. Yu, X. Liu, C. Chen, Q. Chen, J. Ding, A long-acting formulation of a polypeptide drug exenatide in treatment of diabetes using an injectable block copolymer hydrogel, Biomaterials 34 (11) (2013) 2834–2842.
[46] R. Milner, The development of theoretical relationships between some handling parameters (setting time and setting temperature), composition (relative amounts of initiator and activator) and ambient temperature for acrylic bone cement, J. Biomed. Mater. Res. B Appl. Biomater. 68B (2) (2004) 180–185.
[47] X.P. Wang, L. Chen, H. Xiang, J.D. Ye, Influence of anti-washout agents on the rheological properties and injectability of a calcium phosphate cement, J. Biomed. Mater. Res. B Appl. Biomater. 81B (2) (2007) 410–418.
[48] M.-P. Ginebra, C. Canal, M. Espanol, D. Pastorino, E.B. Montufar, Calcium phosphate cements as drug delivery materials, Adv. Drug Deliv. Rev. 64 (12) (2012) 1090–1110.
[49] J. Engstrand, C. Persson, H. Engqvist, The effect of composition on mechanical properties of brushite cements, J. Mech. Behav. Biomed. Mater. 29 (2014) 81–90.
[50] D. Pastorino, C. Canal, M.-P. Ginebra, Multiple characterization study on porosity and pore structure of calcium phosphate cements, Acta Biomater. 28 (2015) 205–214.
[51] J. Wang, C. Liu, Y. Liu, S. Zhang, Double-network interpenetrating bone cement via in situ hybridization protocol, Adv. Funct. Mater. 20 (22) (2010) 3997–4011.
[52] J. Zhang, W. Liu, V. Schnitzler, F. Tancret, J.-M. Bouler, Calcium phosphate cements for bone substitution: Chemistry, handling and mechanical properties, Acta Biomater. 10 (3) (2014) 1035–1049.
[53] I. Lodoso-Torrecilla, J.J.J.P. van den Beucken, J.A. Jansen, Calcium phosphate cements: optimization toward biodegradability, Acta Biomater. 119 (2021) 1–12.
[54] C.C. Chen, D.G. Li, Q.Y. Deng, B.T. Zheng, Optically transparent biocomposites: polymethylmethacrylate reinforced with high-performance chitin nanofibers, Bioresources 7 (4) (2012) 5960–5971.
[55] J.J. Zhu, S.H. Yang, K.W. Cai, S. Wang, Z.Y. Qiu, J.F. Huang, G.Q. Jiang, X. M. Wang, X.Q. Fang, Bioactive poly (methyl methacrylate) bone cement for the treatment of osteoporotic vertebral compression fractures, Theranostics 10 (14) (2020) 6544–6560.
[56] P.H. Cai, S.Y. Lu, J.Q. Yu, L. Xiao, J.Y. Wang, H.F. Liang, L. Huang, G.J. Han, M. X. Bian, S.H. Zhang, J. Zhang, C.S. Liu, L.B. Jiang, Y.L. Li, Injectable nanofiber-reinforced bone cement with controlled biodegradability for minimally-invasive bone regeneration, Bioact. Mater. 21 (2023) 267–283.
[57] S.M. Kenny, M. Buggy, Bone cements and fillers: a review, J. Mater. Sci. Mater. Med. 14 (11) (2003) 923–938.
[58] S.B. Kim, Y.J. Kim, T.R. Yoon, S.A. Park, I.H. Cho, E.J. Kim, I.A. Kim, J.W. Shin, The characteristics of a hydroxyapatite-chitosan-PMMA bone cement, Biomaterials 25 (26) (2004) 5715–5723.
[59] S.L. Teitelbaum, Bone resorption by osteoclasts, Science 289 (5484) (2000) 1504–1508.
[60] L. Wan, H.Y. Song, X. Chen, Y. Zhang, Q. Yue, P.P. Pan, J.C. Su, A.A. Elzatahry, Y. H. Deng, A magnetic-field guided interface coassembly approach to magnetic mesoporous silica nanochains for osteoclast-targeted inhibition and heterogeneous nanocatalysis, Adv. Mater. 30 (25–34) (2018) 9.

[61] H.X. Li, Z.S. Xiao, L.D. Quarles, W. Li, Osteoporosis: mechanism, molecular target and current status on drug development, Curr. Med. Chem. 28 (8) (2021) 1489–1507.
[62] J. Gacanin, A. Kovtun, S. Fischer, V. Schwager, J. Quambusch, S.L. Kuan, W.N. Liu, F. Boldt, C. Li, Z.Q. Yang, D.S. Liu, Y.Z. Wu, T. Weil, H. Barth, A. Ignatius, Spatiotemporally controlled release of Rho-inhibiting C3 toxin from a protein-DNA hybrid hydrogel for targeted inhibition of osteoclast formation and activity, Adv. Healthcare Mater. 6 (21) (2017) 1700392–1700404.
[63] V. Everts, J.M. Delaissé, W. Korper, D.C. Jansen, W. Tigchelaar-Gutter, P. Saftig, W. Beertsen, The bone lining cell:: its role in cleaning Howship's lacunae and initiating bone formation, J. Bone Miner. Res. 17 (1) (2002) 77–90.
[64] J. Landa, N. Margolis, P. Di Cesare, Orthopaedic management of the patient with osteopetrosis, J. Am. Acad. Orthop. Surg. 15 (11) (2007) 654–662.
[65] H. Xie, Z. Cui, L. Wang, Z.Y. Xia, Y. Hu, L.L. Xian, C.J. Li, L. Xie, J. Crane, M. Wan, G.H. Zhen, Q. Bian, B. Yu, W.Z. Chang, T. Qiu, M. Pickarski, L.T. Duong, J. J. Windle, X.H. Luo, E.Y. Liao, X. Cao, PDGF-BB secreted by preosteoclasts induces angiogenesis during coupling with osteogenesis, Nat. Med. 20 (11) (2014) 1270–1278.
[66] T. Ono, T. Nakashima, Recent advances in osteoclast biology, Histochem. Cell Biol. 149 (4) (2018) 325–341.
[67] X. Chen, Z.Q. Wang, N. Duan, G.Y. Zhu, E.M. Schwarz, C. Xie, Osteoblast-osteoclast interactions, Connect. Tissue Res. 59 (2) (2018) 99–107.
[68] J. Wei, C.S. Liu, H. Hong, Y. Yuan, F.P. Chen, Novel biodegradable scaffold of calcium phosphate cement, J. Inorg. Mater. 21 (4) (2006) 958–964.
[69] H. Guo, J. Wei, H. Kong, C. Liu, K. Pan, in: *Biocompatibility and Osteogenesis of Calcium Phosphate Cement Scaffolds for Bone Tissue Engineering*, International Conference on Multifunctional Materials and Structures, Hong Kong, PEOPLES R CHINA, Jul 28-31, Trans Tech Publications Ltd, Hong Kong, PEOPLES R CHINA, 2008, p. 1383, 1296.
[70] F. Bai, G.C. Li, J. Liu, L. Wang, G.L. Meng, H.X. Sang, Comparison of porous calcium acid phosphate cement and titanium alloy scaffold in repairing skull defect of rabbits, Rare Met. Mater. Eng. 39 (11) (2010) 1984–1988.